



HAL
open science

Tuning the spin-orbit coupling, magnetic proximity, and band hybridization in Fe(001)/MgO/MoS₂ multilayers

P. Marcon, R. Arras, D. Li, L. Calmels

► **To cite this version:**

P. Marcon, R. Arras, D. Li, L. Calmels. Tuning the spin-orbit coupling, magnetic proximity, and band hybridization in Fe(001)/MgO/MoS₂ multilayers. *Physical Review B*, 2024, 109 (15), pp.155403. 10.1103/physrevb.109.155403 . hal-04529174

HAL Id: hal-04529174

<https://hal.science/hal-04529174>

Submitted on 2 Apr 2024

HAL is a multi-disciplinary open access archive for the deposit and dissemination of scientific research documents, whether they are published or not. The documents may come from teaching and research institutions in France or abroad, or from public or private research centers.

L'archive ouverte pluridisciplinaire **HAL**, est destinée au dépôt et à la diffusion de documents scientifiques de niveau recherche, publiés ou non, émanant des établissements d'enseignement et de recherche français ou étrangers, des laboratoires publics ou privés.

Tuning the spin-orbit coupling, magnetic proximity, and band hybridization in Fe(001)/MgO/MoS₂ multilayers

P. Marcon,¹ R. Arras,¹ D. Li,¹ and L. Calmels^{1,*}

¹*CEMES, Université de Toulouse, CNRS, 29 rue Jeanne Marvig, F-31055, Toulouse, France*

(Dated: April 2, 2024)

We present first-principles calculations of the electronic structure and spin texture of a MoS₂ monolayer in Fe/MgO/MoS₂ multilayers. These Metal/Insulator/Semiconductor stackings are subject to an electron transfer from the Fe layer to the MoS₂ sheet, giving rise to a two-dimensional (2D) electron gas, the density of which depends on the MgO layer thickness. We describe the consequences of this electron transfer and of the magnetic proximity effect on the occupation of the conduction bands of the MoS₂ layer, on the nature of its band gap, and on the splitting and dispersion of its valence bands near the Γ point of the 2D Brillouin zone. The spin splitting and spin texture are reproduced and understood by an effective Hamiltonian, which includes Rashba, Dresselhaus, and Zeeman effects. We finally show that the splitting of the MoS₂ valence bands induced near Γ by the spin-orbit coupling is rather different when Fe is replaced by a non-magnetic transition metal such as vanadium.

I. INTRODUCTION

Transition-metal dichalcogenide (TMDC) monolayers (MLs) are promising 2D semiconductors which should play a key role in the next generation of electronic, optoelectronic and spintronic devices. They have already been used as the semiconducting channel of field-effect transistors (FETs), with a carrier mobility higher than that measured in the best Si-based devices and with a large ON-OFF current ratio [1–9]. The possibility of designing complex circuits operating logical operations from TMDC-based FETs has further been reported in several articles [10–12]. Their optical properties have also been exploited in different kinds of optoelectronic devices [13], ranging from solar cells [14] to photovoltaic and photo-detecting devices [15, 16], phototransistors [17–19], photodiodes [14] and light emitting diodes [12]. The use of TMDC layers in spintronic devices has also been considered by different theoretical and experimental teams. Magnetic tunnel junctions (MTJs) based on a non-magnetic and insulating TMDC spacer and different kinds of magnetic electrodes have thus been studied [20–31]. More complicated stackings have also been considered for spintronic applications, like the Fe/MoS₂/Phosphorene/Pt multilayer, of which the spin-transfer-torque properties have recently been calculated from first principles [32]. TMDC-based stacks have finally been studied for their possible spin-orbitronics applications. Most of the corresponding studies focused on charge-to-spin conversion at the graphene/TMDC interfaces [33–44], where the TMDC layers are mainly used to provide strong spin-orbit coupling (SOC) effects to the charge carriers supplied by the graphene layer. A large spin-orbit torque effect has also been observed at the TMDC/CoFeB interface, which is potentially interesting for its spin/charge conversion properties [45].

The key role played by TMDC MLs in all these devices is mostly due to the very interesting specificities of their uncommon band structure. Experiments have indeed evidenced that their band gap is direct [46, 47]. This has been confirmed by calculations based on first-principles or tight-binding methods, which have shown that the direct band gap occurs at the 6 K points of the first Brillouin zone (BZ) [46]. Calculations have also shown that the combination of the SOC and lack of inversion symmetry induces a large spin splitting of their valence bands and a smaller but non-negligible spin splitting of their conduction bands at the K valleys [48], with an intimate coupling between the spin and valley degrees of freedom. This coupling splits the 6 valleys of the TMDC MLs in two degenerated groups with opposite spin splittings, respectively located at the three K and three K' Bloch vectors [49–51]. Absorption of circularly-polarized photons has moreover been used to selectively populate the K or K' valleys with electrons and holes [52–55], evidencing that light can be used to perfectly control the TMDC ML valley degree of freedom.

Several authors have further shown that different kinds of external stimuli may be used to control the nature and the energy width of the band gap of a TMDC ML. First-principles calculations have for instance shown that a sufficiently large strain can switch the band gap from direct at K/K' to indirect between Γ and K/K' [56–62]. A similar switch of the top of the valence band has also been reached by applying an external electric field [63–66], or by creating an interface between the TMDC ML and either an oxide like EuO [67], or MgO-terminated multilayers [68]. Moreover, different strategies have been investigated for lifting the degeneracy between the bands with opposite spin states respectively located at the K and K' valleys, starting with the use of an external magnetic field applied perpendicular to the TMDC layer, thus inducing a Zeeman splitting of the inequivalent valleys [69–75]. Another route, more attractive from the perspective of designing TMDC ML-based devices operating without applying an external magnetic field, has consisted in us-

* lionel.calmels@cemes.fr

ing interfaces between TMDC and ferromagnetic layers. In this case, the lift of the valley degeneracy is induced by the exchange magnetic field provided by the proximity of the ferromagnet. Different magnetic materials have been considered to reach this aim [20, 45, 67, 76–97]. Interfaces involving covalent bonds between a TMDC layer and a magnetic metal generally fail in preserving the semiconducting character of the TMDC layer [85]. Conversely, these layers remain semiconducting and their valley degeneracy is generally lifted when they are bound by van der Waals (vdW) interaction, either directly to the magnetic layer or through a single h-BN layer intercalated between the TMDC and the ferromagnet [98].

The band structure of a single TMDC layer can finally be modified by the Rashba interaction [99–104] which induces additional lifts of the spin degeneracy near the top of the valence band at Γ . This occurs for Janus TMDC layers with different kinds of chalcogen atoms on the two sides of the metallic atom layer [105–111], but also when an external electric field is applied perpendicular to a non-polar TMDC ML [9, 64–66, 72, 75] or to a Janus TMDC layer [108, 109]. Last, a Rashba spin splitting of the TMDC valence band near Γ has also been observed at the interfaces between a TMDC layer and a Bi surface [112] or at the the interface between two different TMDC layers [113]; in these cases, the Rashba effect is due to the interface built-in electric field and to the non-negligible hybridization that occurs across the interface. The spin splitting of the valence bands near Γ and the related spin texture induced by Rashba-like SOC effects could allow controlling the spin properties of TMDC-based spin-orbitronics devices with an electric instead of a magnetic field, in particular when the splitting is strong or when the SOC induces a persistent spin texture. Indeed, such a unidirectional spin polarization of the TMDC electron states in the \mathbf{k} -space should give access to the long carrier spin lifetime required to control the spin orientation [114].

With this scientific and technological context in mind, we have calculated the electronic structure and the magnetic properties of Fe(7MLs)/MgO(n MLs)/MoS₂(1ML) multilayers made of a thin Fe ferromagnetic layer with perpendicular magnetic anisotropy, an insulating MgO layer with a thickness t_{MgO} between 3 and 7 MLs and a single MoS₂ layer. Such a stacking, which has recently been synthesized with a 1.5 nm thick MgO layer [68], allows simultaneously switching the MoS₂ band gap (from direct to indirect) and to increase the magnetic proximity effects when the MgO thickness is lowered. Moreover, decreasing the MgO thickness also changes the MgO/MoS₂ interface built-in electric field and the subsequent strength of the interface-induced SOC. It finally modifies the energy offset between the MgO and MoS₂ bands, possibly leading to different band hybridizations at the MgO/MoS₂ interface.

We present a systematic study of the band structure of these multilayers, with a particular focus on the lift of the spin degeneracy and on the spin texture near the

valence band maximum at Γ , which we have studied as a function of the MgO layer thickness. Our first-principles data are fitted with a simple phenomenological Hamiltonian model that includes exchange Zeeman, Rashba and Dresselhaus interactions, a possible shift of the valence band maximum and a possible modification of the effective mass. We used this model to evaluate the relative weights of the Zeeman, Rashba and Dresselhaus contributions and understand which of these effects govern the properties of the MoS₂ layer, as a function of the MgO thickness. We also show that the model fails at critical MgO thicknesses for which the dispersion of the valence band near Γ is governed by band-hybridization between MgO and MoS₂, giving rise to persistent spin textures. We finally compare the SOC effects calculated for the Fe/MgO/MoS₂ multilayers with those computed for non-magnetic V/MgO/MoS₂ systems.

II. CALCULATION METHODS

As shown in Fig. 1, we used supercells consisting of asymmetric Fe(7MLs)(001)/MgO(001)/1H-MoS₂ multilayers stacked along the z direction and with t_{MgO} between 3 and 7 MLs. We only studied multilayers based on the 1H-MoS₂ ML, which is considered as the most stable one and is potentially interesting for electronic applications due to its semiconducting behaviour (whereas the 1T-MoS₂ phase is metallic). In genuine Fe/MgO/MoS₂ samples, the MoS₂ layer and the Fe/MgO bilayer both keep their own in-plane lattice parameters, MoS₂ being only bound by the weak vdW interaction to the rest of the stacking. Supercells with a perfect matching would contain a huge number of non-equivalent atoms, due to the periodic boundary conditions. Calculating their electronic structure from first principles would be too computationally demanding. As we mainly wish to understand how electron states of the MoS₂ single layer are modified by the interface with Fe/MgO, we chose to use orthorhombic-shaped supercells with the lattice parameters $a_1 = a_{\text{MoS}_2}$ and $a_2 = \sqrt{3}a_{\text{MoS}_2}$, respectively along the x and y directions. This choice preserves the hexagonal structure and the lattice parameter $a_{\text{MoS}_2} = 3.16 \text{ \AA}$ calculated for the isolated 1H-MoS₂ sheet at equilibrium, while limiting the number of atoms contained in the supercell. The price to pay is the resulting structural distortion of the Fe/MgO bilayer, which loses its square-shaped aspect leading, in MgO, to a tensile strain of 6.5% along the x axis (where the distance between Mg atoms is stretched from $a_{\text{MgO}}/\sqrt{2}$ to a_1) and to a compressive strain of -7.8% along the y axis (where the distance between second neighbor Mg atoms is compressed from $\sqrt{2}a_{\text{MgO}}$ to a_2). Strains are also applied to the Fe layer, a_{Fe} being stretched to a_1 and $2a_{\text{Fe}}$ compressed to a_2 , respectively in the x and y directions. We checked that such structural distortions do not drastically change the electronic structure of the bulk Fe and MgO crystals (see Figs. S1 and S2 in the supplement-

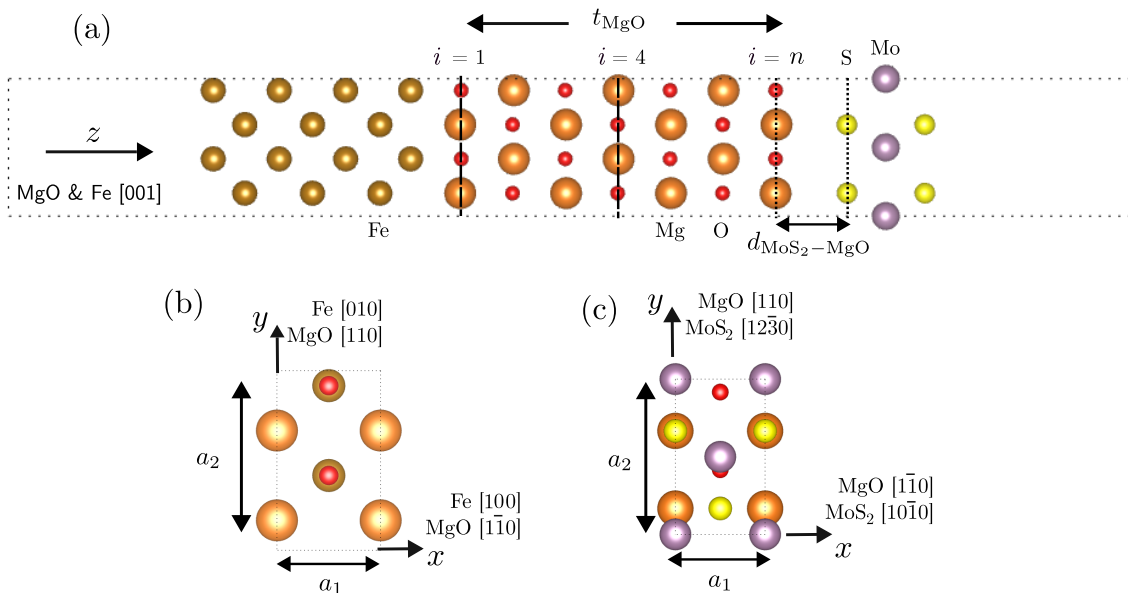


FIG. 1. Atomic structure of the Fe/MgO(n MLs)/MoS₂ supercells: (a) Side view and plane views of (b) the Fe/MgO and (c) MoS₂/MgO interfaces.

tary materials file [115]). Indeed, even if the distortions split some of the energy bands that would otherwise be degenerated, the density of states (DOS) curves are not drastically changed by the distortions: the Fermi level E_F still crosses the d bands of the Fe crystal and the band gap of MgO. As shown previously [116], the atomic structure with the lowest energy is found when O atoms are located on top of Fe atoms at the Fe/MgO interface, while 2/3 of the S atoms are on top of half of the Mg atoms at the MgO/MoS₂ interface [68], see Fig. 1.

A vacuum space of about 16 Å was taken in order to avoid unphysical interactions between two neighboring slabs in the z direction. A dipole correction [117] was added to cancel any spurious electric field created between facing surfaces. Internal coordinates were optimized using a conjugate gradient algorithm, until all forces were less than 10^{-2} eV/Å.

First-principles calculations of the physical properties of the Fe/MgO/MoS₂ multilayers were performed with the supercells described above and the VASP code [118–121] based on density-functional theory (DFT) and on the projector augmented wave (PAW) method [122]. The energy cutoff was set to 550 eV. All DFT calculations have been done at the Perdew-Burke-Ernzerhof (PBE) level [123]. We also took into account vdW interactions using the Grimme correction [124].

SOC was added self-consistently in electronic structure calculations [125]. The 2D first BZ was sampled with a $20 \times 16 \times 1$ Monkhorst-Pack grid [126] for optimizing the structure and for calculating the DOS curves. Subsequently, the band-structure and spin texture post-processing were done using the python library

PYPROCAR [127].

The built-in electric field in the MgO layers has been estimated from the ratio $|V(z_L) - V(z_R)|/(z_R - z_L)$, where $V(z_L)$ and $V(z_R)$ are the values of the (xy) -planar averaged electrostatic potential calculated at the second and penultimate MgO MLs. This method, which should give more reliable results for thicker MgO layers, as it avoids taking into account the sharp variations of the electrostatic potentials at the two interfacial MgO MLs, has been applied to the multilayers with $4 \text{ MLs} \leq t_{\text{MgO}} \leq 7 \text{ MLs}$. For the system with $t_{\text{MgO}} = 3 \text{ MLs}$, for which interface effects cannot be avoided, we estimated the electric field at the center of the MgO layers from the values $V(z_L)$ and $V(z_R)$ calculated at the first and third MgO MLs.

Parameters used in the effective Hamiltonian proposed in Sec. III B 3 were fitted from energy bands calculated near the center Γ of the BZ and along the k_x or k_y directions, using 30 Bloch wave vectors between $k_{x(y)} = -0.06 \text{ \AA}^{-1}$ and $+0.06 \text{ \AA}^{-1}$.

III. MgO-THICKNESS DEPENDENCE OF THE ELECTRONIC STRUCTURE AND OF THE SPIN TEXTURE

A. Overview of the results obtained for Fe/MgO(7MLs)/MoS₂

We first briefly summarize and complete the results that we have recently reported for the multilayer with $t_{\text{MgO}} = 7 \text{ MLs}$ [68], the largest MgO layer thickness that

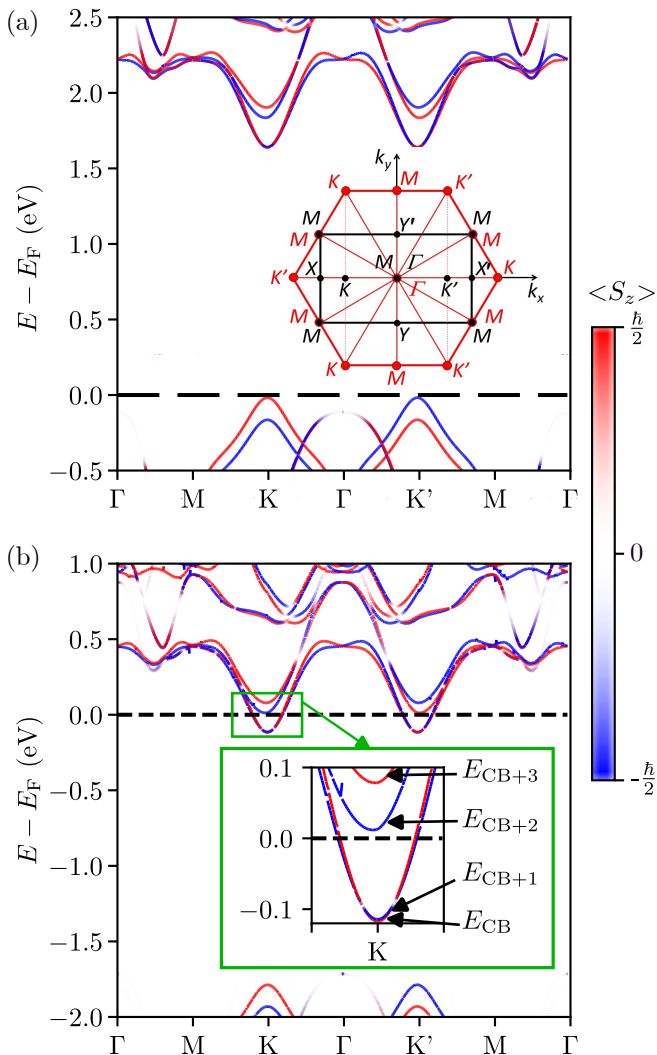


FIG. 2. Spin-projected band structure along the high-symmetry directions of the rectangular BZ of the supercell shown in Fig. 1, for (a) an isolated 1H-MoS₂ ML and (b) the MoS₂ ML in the Fe/MgO(7MLs)/MoS₂ multilayer. The rectangular first BZ of the multilayer is represented in panel (a) with black lines and black letters, where it is compared to the hexagonal BZ of the isolated MoS₂ layer (in red).

we will consider here. This system will further be used as a reference when we will describe the increase of the SOC and magnetic proximity effects induced by the decrease of the MgO spacer thickness.

For Fe/MgO(7MLs)/MoS₂, the average distance $d_{\text{MoS}_2\text{-MgO}}$ calculated between the interface S and MgO layers (see Fig. 1.a) is of 2.84 Å, a value comparable to that recently reported for the Ga₂O₃/MoS₂ interface [128]. This confirms that the MoS₂ layer is bound to the rest of the stacking by weak vdW interaction.

The electronic structure of MoS₂ in Fe/MgO(7MLs)/MoS₂ shows strong similarities with that of the isolated MoS₂ ML, the overall dispersion of the MoS₂ bands being globally preserved in the

multilayer, but noticeable differences appear as shown in Fig. 2. In particular, the MoS₂ band gap is no longer direct at K/K', but becomes indirect from Γ to K/K', due to non-negligible orbital interactions across the MoS₂/MgO interface, as it will be discussed further on. Moreover, the difference between the work function of the (001) Fe surface (3.95 eV calculated for the surface of the distorted Fe crystal, 4.17 eV measured experimentally [129]) and the electron affinity of MoS₂ (4.20 eV according to our calculations, 4.3 eV [130] and 4.7 eV [131] measured in experiments) results in an electron transfer from the Fe/MgO interface to the MoS₂ layer, rising E_F above the minimum of the two MoS₂ conduction bands with the lowest energy at K/K' (these bands are labeled CB and CB+1 in Fig. 2).

The transferred electrons occupying these bands form a two-dimensional electron gas (2DEG) with an effective mass of 0.774 m_0 along Γ -K (m_0 being the mass of the free electron) and an electron density n_e of 0.0543 electron per $\sqrt{3}a_{\text{MoS}_2}^2$ area. This 2DEG is not spin polarized, magnetic proximity effects being insufficient to strongly lift the degeneracy between the MoS₂ conduction bands with opposite spin directions at K and K'. Conduction bands with a higher energy (CB+2 and CB+3 in Fig. 2) have their minima at K/K' above E_F for this multilayer. These minima correspond to the conduction-band minima located at the 6 Q-points of the hexagonal primitive-cell BZ of the isolated MoS₂ layer (i. e. halfway between Γ and K/K'). After building the supercell shown in Fig. 1, the minima of CB, CB+1, CB+2 and CB+3 are folded at the same point of the rectangular conventional cell BZ, see Fig. 2.

The charge transferred across the MgO layer creates an internal electric field $E_{\text{int}} = 0.12$ V/Å, which induces Mg-O polar displacements along the [001] direction: we found $\delta z = \{ \langle z_{\text{Mg}^{2+}} \rangle - \langle z_{\text{O}^{2-}} \rangle \} = 0.04$ Å at the center of the MgO layer. This electric field is of the same order of magnitude as the field $\frac{n_e}{\epsilon_r \epsilon_0} = 0.057$ V/Å that would exist in a capacitor with charge densities $\pm en_e$ on its plates and a spacer material with the same dielectric constant $\epsilon_r = 9.83$ as that of MgO [132]. This capacitor model, however, assumes a homogeneous spacer material and two-dimensional charge distributions with a thickness negligible compared to t_{MgO} , which should not be the case for the systems with very thin MgO layers that we considered here (this could explain the difference between the values that we calculated and those given by the capacitor model).

Even if magnetic proximity effects are small for the MgO thickness of 7 MLs, they are responsible for a significant 0.24 meV spin splitting of the MoS₂ valence band maximum at Γ . Finally, Fig. 2 shows that the spin direction for electron states near the top of the valence band at Γ tilts from out-of-plane for the isolated MoS₂ layer to in-plane for MoS₂ in Fe/MgO(7MLs)/MoS₂.

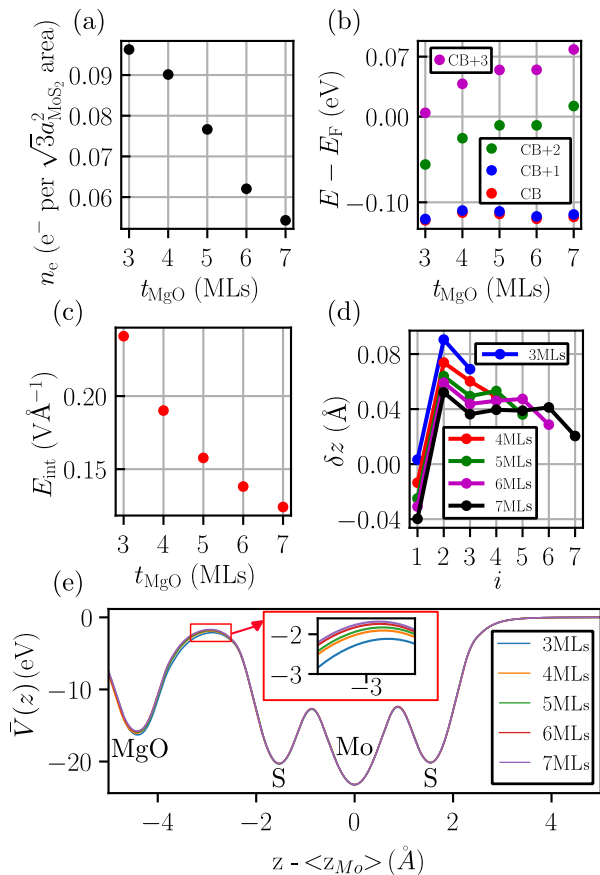


FIG. 3. (a) Electron density n_e of the 2DEG occupying the conduction bands of the MoS₂ layer, versus the MgO layer thickness. (b) Energy of the successive conduction band minima at K/K', versus MgO layer thickness. (c) Internal electric field E_{int} at the center of the MgO layer, versus MgO layer thickness. (d) Mg-O buckling δz versus index i of the MgO atomic layer ($i = 1$ corresponding to the MgO ML at the Fe/MgO interface) and for different thicknesses of the MgO layer. (e) (xy) -planar averaged electrostatic potential in the vicinity of the MoS₂ ML, as a function of the z coordinate and for different values of the MgO layer thickness (the inset shows the values of the potential in the vdW gap at the MgO/MoS₂ interface).

B. Tuning the MoS₂ electronic structure by decreasing the MgO layer thickness

We now describe the modification of the electronic properties of the MoS₂ ML induced by a lowering of the MgO layer thickness, focusing on the MoS₂ conduction bands near K/K' and valence bands near Γ .

1. Occupancy and spin splitting of the MoS₂ conduction bands at K/K'

The electron density n_e of the 2DEG transferred from the Fe electrode to the MoS₂ ML has been calculated by

integrating the Mo- and S-atom partial charge densities corresponding to the occupied part of CB, CB+1 and CB+2. Fig. 3(a) shows that n_e monotonously increases from 0.0543 to 0.0963 electron per $\sqrt{3}a_{\text{MoS}_2}^2$ area, when the MgO-layer thickness decreases from 7 to 3 MLs. This increase is mainly due to the pulling down below E_F of the minimum of the conduction band CB+2. This can be seen in Fig. 3(b), where we plotted the energy of the conduction band minima of CB, CB+1, CB+2 and CB+3, as a function of the MgO layer thickness. The energy shift induced by a lowering of the MgO layer thickness is not rigid: The energy (with respect to E_F) of the minimum of the conduction bands CB and CB+1 and the number of electrons populating these two bands are nearly independent of t_{MgO} . On the other hand, the energy of the CB+2 and CB+3 conduction band minima tends to decrease (and the population of CB+2 to increase) when the thickness of the MgO layer is lowered.

As explained in Sec. III A, an internal electric field E_{int} appears in the MgO dielectric layer due to the electron transfer from the Fe electrode to the MoS₂ ML. The value of E_{int} calculated at the center of the MgO layer is represented in Fig. 3(c) as a function of the MgO layer thickness. It increases from 0.12 $\text{V}\text{\AA}^{-1}$ for $t_{\text{MgO}} = 7$ MLs to 0.24 $\text{V}\text{\AA}^{-1}$ for $t_{\text{MgO}} = 3$ MLs and the variation of E_{int} with the MgO-layer thickness is more or less proportional to n_e , as it would be the case for the simple capacitor model.

The Mg-O buckling δz is represented in Fig. 3(d) as a function of the MgO atomic layer index i and for $t_{\text{MgO}} = 3 - 7$ MLs. Except at the Fe/MgO interface, this buckling is positive, which corresponds to the expected displacement of the Mg cations in the direction of the internal electric field (i.e. towards MoS₂) and of the O anions in the opposite direction (towards Fe). The value of the buckling at the center of the MgO layer increases with the internal electric field, from 0.04 \AA for $t_{\text{MgO}} = 7$ MLs to 0.09 \AA for $t_{\text{MgO}} = 3$ MLs.

The difference between the xy -planar averaged electrostatic potentials $\bar{V}(z)$ calculated near the MoS₂ layers of multilayers with different values of the MgO thickness is very small, except in the vdW gap between the top MgO and interface S atomic layers, as shown in Fig. 3(e). As it will be explained later, the associated increase of the electric field in the vdW gap will be responsible for the enhancement of the SOC effects.

We finally turn our attention to the effects of the MgO layer thickness on the spin splitting of the conduction bands mostly induced by SOC at each of the K and K' valleys, and on the valley Zeeman splitting induced between the K and K' valleys by magnetic proximity effects. The spin splitting of the conduction bands decreases from 3 meV for $t_{\text{MgO}} = 7$ MLs (a value close to that reported in Ref. [50] for the isolated MoS₂ layer) to 1.6 meV for $t_{\text{MgO}} = 3$ MLs. The valley Zeeman splitting of the conduction bands is of 0.6 meV for $t_{\text{MgO}} = 3$ MLs, i.e. for the thickness at which the magnetic proximity effects are the strongest; this value corresponds to an effective magnetic

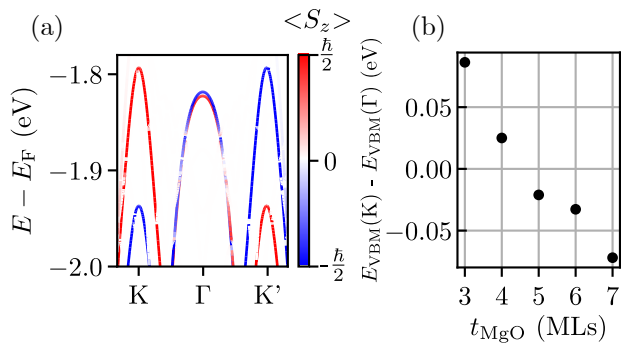


FIG. 4. (a) Contribution of the MoS₂ ML to the highest-energy valence bands of Fe/MgO(4MLs)/MoS₂. (b) Energy difference between the top of the valence bands at K and Γ , as a function of the MgO layer thickness.

field of a few Tesla. It becomes negligible and difficult to accurately calculate for thicker MgO layers. It may be too small to be measured experimentally.

2. Nature of the MoS₂ band gap

The switchover of the MoS₂ band gap, from direct (at K/K') for an isolated MoS₂ layer to indirect (from Γ to K/K') for a MoS₂ ML in a Fe/MgO/MoS₂ multilayer, occurs above a critical MgO layer thickness. Fig. 4(a) shows the dispersion of the MoS₂ valence bands for $t_{\text{MgO}} = 4$ MLs, the largest MgO thickness for which the band gap of MoS₂ is direct. The difference between the energies of the valence band maxima (VBM) calculated at K/K' and at Γ is plotted in Fig. 4.(b) as a function of the MgO layer thickness: it is negative for $t_{\text{MgO}} \geq 5$ MLs, from which the band gap becomes indirect. This is mainly due to a 0.16 eV decrease of the energy difference [$E_{\text{CBM}}(\text{K/K}') - E_{\text{VBM}}(\Gamma)$] between the conduction band minimum (CBM) at K/K' and the VBM at Γ , when t_{MgO} increases from 3 to 7 MLs, while the energy difference [$E_{\text{CBM}}(\text{K/K}') - E_{\text{VBM}}(\text{K/K}')$] is nearly independent of the MgO layer thickness. These observations are not surprising: the top of the valence band at Γ mainly involves Mo- d_{z^2} and S- p_z atomic orbitals, the latter being very sensitive to the presence of neighboring atomic layers (i.e. to the thickness of the MgO layer), while the CBM and VBM at K/K' do not involve contributions from S- p_z atomic orbitals.

Several interdependent driving forces can be cited to explain that the contribution of the p_z orbitals of the interface S atoms and the energy of the MoS₂ VBM at Γ change with t_{MgO} . First, the energy (and the number) of the MgO valence bands depend on the thickness of the MgO layer, in particular when it becomes ultrathin. Furthermore, the energy of the MgO bands is also shifted by the internal electric field induced in all the MgO atomic layers by the charge transfer from Fe to

MoS₂. Finally, as we will discuss below, an hybridization between Mo, S, Mg and O atomic orbitals occurs when the MgO and MoS₂ valence bands have similar energies. These arguments suggest that changes in the MoS₂ VBM at Γ should better be due to thickness-dependent interactions with MgO bands, than to a modification of the width of the vdW gap, which stays nearly constant, around 2.85 Å (except maybe for $t_{\text{MgO}} = 3$ MLs, for which it slightly decreases down to 2.8 Å).

3. Splitting and dispersion of the valence bands near Γ

Fig. 5 shows the dispersion near the top of the MoS₂ valence bands at Γ , calculated for Fe/MgO(n MLs)/MoS₂ multilayers with different MgO layer thicknesses. The two bands in this figure are splitted by the SOC and magnetic proximity effects. The dispersion and band splitting computed along Γ -X are similar to those calculated from a simple model of a 2DEG immersed in a perpendicular exchange magnetic field and with Rashba-like SOC. Indeed, the top panels of Fig. 5 corresponding to $t_{\text{MgO}} = 7$ MLs and to $t_{\text{MgO}} = 3 - 6$ MLs are respectively similar to those displayed in Refs. [104, 133–136] for a Zeeman effect smaller than SOC effects, and in Refs. [134, 136] for SOC effects smaller than the Zeeman one.

Fig. 5 shows that the spin splitting induced at Γ by the exchange magnetic field continuously increases when the MgO-layer thickness decreases, from 0.24 meV for $t_{\text{MgO}} = 7$ MLs to 7.2 meV for $t_{\text{MgO}} = 3$ MLs. This splitting could be measured by angle-resolved photoemission spectroscopy (ARPES), providing that spectra can be recorded with a sufficient resolution. Fig. 5 also shows that the dispersion of the valence bands is not isotropic, with a band curvature bigger along Γ -Y than along Γ -X (two different effective masses m_x^* and m_y^* are necessary to describe the dispersion). This anisotropy is a consequence of the anisotropy of the structure of the MgO/MoS₂ interface (see Fig. 1.c), where the hexagonal MoS₂ and the rectangular top MgO MLs are juxtaposed.

The valence-band dispersion and spin splitting are different for $t_{\text{MgO}} = 7$ and 3 MLs than for $t_{\text{MgO}} = 4, 5$ and 6 MLs. Indeed, Fig. 5 shows that the valence bands become unexpectedly flat along Γ -Y for $t_{\text{MgO}} = 7$ MLs. For $t_{\text{MgO}} = 3$ MLs, the MoS₂ ML actually contributes to 4 different electron bands instead of 2, in a small energy range of 26 meV near the top of the valence bands at Γ ; only the two bands with the lowest energy and the highest MoS₂ contributions are shown in Fig. 5. We will see in the next section that the specific band dispersion observed for $t_{\text{MgO}} = 3$ and 7 MLs are a consequence of the hybridization and interaction between the valence bands of MoS₂ and of MgO.

We used an effective Hamiltonian to reproduce the band structure, considering that the splitting near Γ of the highest energy valence bands has two main sources: (1) the SOC which manifests itself, in this system with broken inversion symmetry, through a combination of the

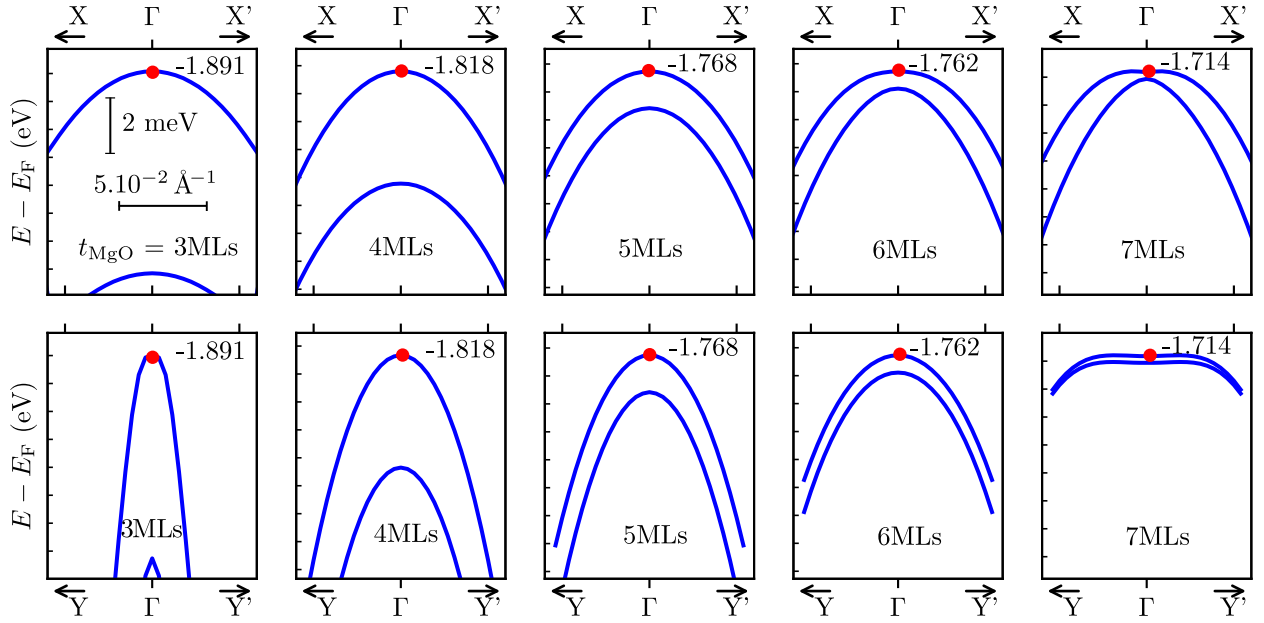


FIG. 5. Dispersion of the MoS₂ valence bands near the VBM at Γ , calculated from first principles for Bloch wave vectors along the Γ -X direction (upper panels) and along the Γ -Y direction (lower panels). The different panels correspond to Fe/MgO/MoS₂ multilayers with $t_{\text{MgO}}=3, 4, 5, 6$ and 7 MLs. The energy of the VBM at Γ (indicated by a red dot) is given in each panel.

Rashba and Dresselhaus effects and (2) the Zeeman effect due to the proximity of the Fe ferromagnetic layer. To estimate the relative contributions of the Rashba, Dresselhaus and Zeeman effects, we fitted the band structure near the top of the valence bands at Γ computed from first principles, with the eigenvalues that we calculated for an effective Hamiltonian taking all these effects into account [137, 138]. This Hamiltonian is given by

$$\hat{H} = \hat{H}_0 + \hat{H}_R + \hat{H}_D + \hat{H}_Z, \quad (1)$$

where

$$\hat{H}_0 = \epsilon \hat{I} + \frac{\hat{p}_x^2}{2m_x^*} + \frac{\hat{p}_y^2}{2m_y^*} \quad (2)$$

describes a free 2DEG with a non-isotropic dispersion (m_x^* and m_y^* are the effective masses, respectively along the x and y directions, \hat{I} is the identity matrix and ϵ is an offset energy). Because of the non-trivial crystal structure of the slabs and interfaces described here, the little point group associated with Γ is C_s , which only possesses two symmetry elements: the identity and a (100) mirror plane. Several non-equivalent terms, invariant by this small number of symmetry elements, could contribute to the SOC effect in a Hamiltonian model. Considering the splitting of the valence bands near Γ , we have chosen to approximate the SOC part of the Hamiltonian by only keeping the terms corresponding to the standard two-dimensional linear Rashba and Dresselhaus interactions

[100, 137, 139]:

$$\hat{H}_R = \alpha(k_y \hat{\sigma}_x - \hat{\sigma}_y k_x) \quad (3)$$

and

$$\hat{H}_D = \beta(k_y \hat{\sigma}_x + \hat{\sigma}_y k_x). \quad (4)$$

\hat{H}_R and \hat{H}_D depend on the x and y components of the Pauli matrix $\hat{\sigma}$ and wave vector \mathbf{k} . α and β are respectively the 2D Rashba and Dresselhaus coefficients. We further demonstrate that these two terms, respectively induced by the built-in electric field due to charge reorganization near the MgO/MoS₂ interface and by the xy -crystalline anisotropy of this interface, indeed suffice to describe most of the consequences of SOC calculated from first principles, thus gathering the most important physical elements necessary to explain the properties of Fe/MgO/MoS₂ multilayers. We checked that cubic SOC terms are negligible for small Bloch-vector ranges near Γ [140]. The Zeeman term, which accounts for magnetic proximity effects, is given by

$$\hat{H}_Z = \mu_B B \hat{\sigma}_z \quad (5)$$

where B is the modulus of the effective exchange magnetic field oriented along the z axis. We have restricted our description of the Hamiltonian to these few contributions only, which correctly account for the small wave

| t_{MgO} | 4MLs | 5MLs | 6MLs |
|------------------|--------|--------|--------|
| ϵ (eV) | -1.82 | -1.77 | -1.76 |
| m_x^*/m_0 | -3.542 | -3.263 | -3.121 |
| m_y^*/m_0 | -1.191 | -1.475 | -2.35 |
| α (meVÅ) | 11.27 | 3.98 | -5.07 |
| β (meVÅ) | 22.34 | 18.23 | 13.95 |
| $\mu_B B$ (meV) | 2.0 | 0.66 | 0.31 |

TABLE I. Parameters of the effective Hamiltonian fitted from the MoS₂ band structure and spin texture calculated from first principles near the top of the valence bands at Γ , for Fe/MgO/MoS₂ multilayers with $t_{\text{MgO}} = 4, 5$ and 6 MLs.

vector dependence of the MoS₂ valence band spin splitting near Γ for 4 MLs $\leq t_{\text{MgO}} \leq 6$ MLs, as the MoS₂ valence bands neither hybridize nor strongly interact with MgO bands in this case. The effective Hamiltonian would be more complicated out of this MgO thickness range: It should contain more terms to go beyond the simple parabolic dispersion and include the description of both the MoS₂ and MgO hybridized bands, which is out of the scope of the present article.

The diagonalization of \hat{H} gives access to the dispersion of the splitted bands:

$$E_{\pm} = \epsilon + \frac{\hbar^2 k_x^2}{2m_x^*} + \frac{\hbar^2 k_y^2}{2m_y^*} \pm \sqrt{(\alpha - \beta)^2 k_x^2 + (\alpha + \beta)^2 k_y^2 + (\mu_B B)^2}. \quad (6)$$

Table I gives the value of the parameters ϵ , m_x^* , m_y^* , α , β and $\mu_B B$ obtained by fitting the energies of the MoS₂ band structures calculated from first principles near the top of the valence band at Γ with Eq. 6. This table shows that the SOC coefficients (α and β) and the exchange Zeeman proximity effect ($\mu_B B$) all increase when the MgO thickness decreases. The spin splitting calculated at Γ ($2\mu_B B = 4$ meV for $t_{\text{MgO}} = 4$ MLs) is due to the exchange effect induced by the proximity of the ferromagnetic layer and of the tail of its spin-polarized electron wave functions, which decreases exponentially in the thin MgO layer. β is always larger than α (however, this latter is never negligible). The spin-orbit coefficients α and β that we calculated have the same order of magnitude as the Rashba coefficient computed for a single MoS₂ layer in a perpendicular electric field of 0.1 V/Å [64]. However, such a Hamiltonian model is not suitable to describe the band structure for multilayers with $t_{\text{MgO}} = 3$ and 7 MLs, hybridization effects being stronger in these cases, as it will be discussed in the next section.

The comparison between the first-principles results and the analytical equations corresponding to the Hamiltonian model is shown in Appendix A).

4. Hybridization of the valence bands near Γ

The contributions to the band structure of the MoS₂ and of its first-neighbor MgO MLs are compared in Fig. 6, with an energy scale larger than in Fig. 5 (the splitting near the top of the MoS₂ valence bands discussed in Sec. III B 3 is not visible at this scale). This figure explains why the MoS₂ valence bands show a different dispersion along Γ -Y and Γ -X: this is mostly due to the presence of MgO bands which are more dispersive along Γ -Y than along Γ -X. Due to this stronger dispersion, the highest energy MoS₂ valence bands and MgO surface bands do overlap along Γ -Y, displaying an anticrossing that locally affects the dispersion of the MoS₂ bands.

The highest-energy interface-MgO bands shift downwards when t_{MgO} decreases. This is partly due to the value of the potential jump between the Fe/MgO and the MgO/MoS₂ interfaces, which is found smaller for thinner than for thicker MgO layers, despite higher values of the electric field in the MgO layer. The interface MgO band reaches the MoS₂ valence band maximum at Γ for $t_{\text{MgO}} = 3$ MLs, giving rise to a strong hybridization near Γ , between the two splitted MoS₂ valence bands and two (one for each spin state) MgO bands.

A second MgO band can finally be observed at lower energies in this figure. Although the interface MgO ML contributes less to this band (which only appears as a light line in Fig. 6), its presence slightly modifies the dispersion of the MoS₂ valence bands for $t_{\text{MgO}} = 7$ MLs. For this MgO-layer thickness, the difference between the energies of the MgO and MoS₂ bands becomes smaller near Γ and the MoS₂ bands lose their parabolic shape, in particular along Γ -Y, due to orbital interactions across the vdW gap.

5. Spin texture of the MoS₂ valence bands near Γ

This section describes the Bloch-vector and MgO-thickness dependences of the direction of the spin vector, for the two highest-energy valence bands shown in Fig. 5. We only describe the spin texture of the multilayers with $t_{\text{MgO}} = 4, 5, 6$ and 7 MLs.

Fig. 7 shows the variations of the angle θ between the spin vector and the z axis, calculated for the two highest energy-splitted MoS₂ valence bands, for small Bloch vectors along Γ -X and Γ -Y and for different values of the MgO layer thickness. The spin, for these two valence bands, is always perpendicular to the MoS₂ layer at the center Γ of the BZ ($\theta = 0$ or π). The component of the spin vector perpendicular to the MoS₂ layer decreases when the Bloch vector increases along Γ -X (see the top panels in Fig. 7), at the benefit of its in-plane projection. This rotation of the spin from mostly out-of-plane at Γ to mostly in-plane far from Γ occurs at smaller Bloch vectors for the thicker MgO layers. This is due to the fact that magnetic proximity effects, which tend to align the

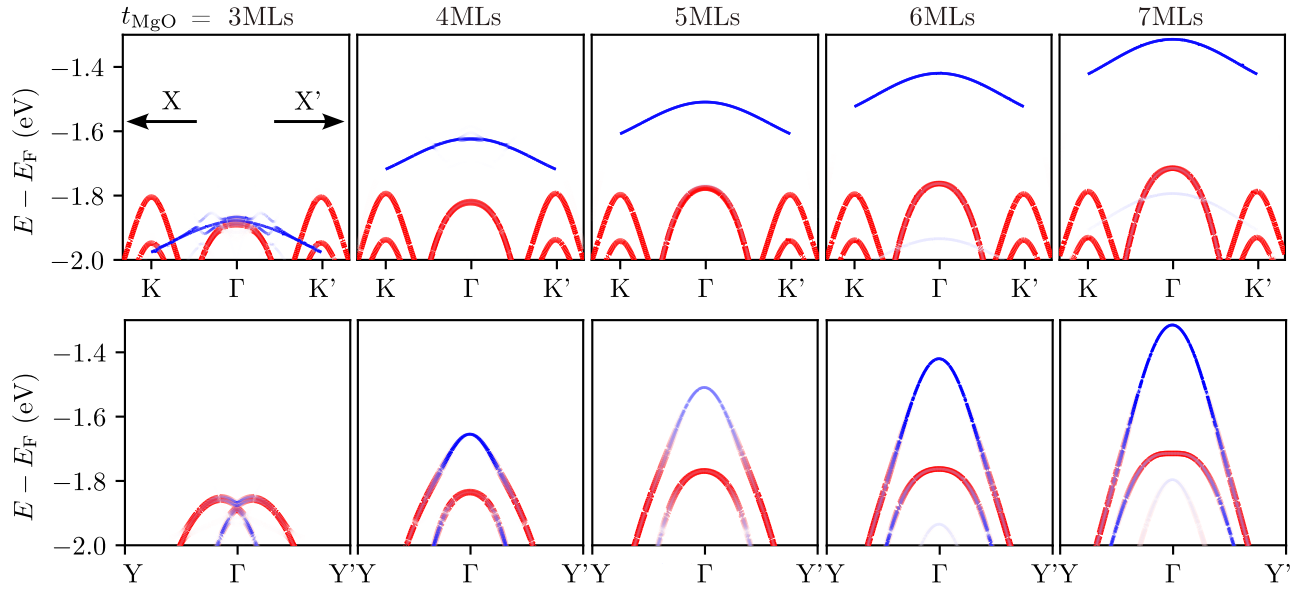


FIG. 6. Contributions of the MgO interface ML (blue lines) and of the MoS₂ ML (red lines) to the valence bands of the Fe/MgO/MoS₂ multilayers, for $t_{\text{MgO}} = 3, 4, 5, 6$ and 7 MLs and for Bloch wave vectors along the Γ -X (upper panels) and Γ -Y (lower panels) directions. The K/K' points are located between Γ and the X/X' points.

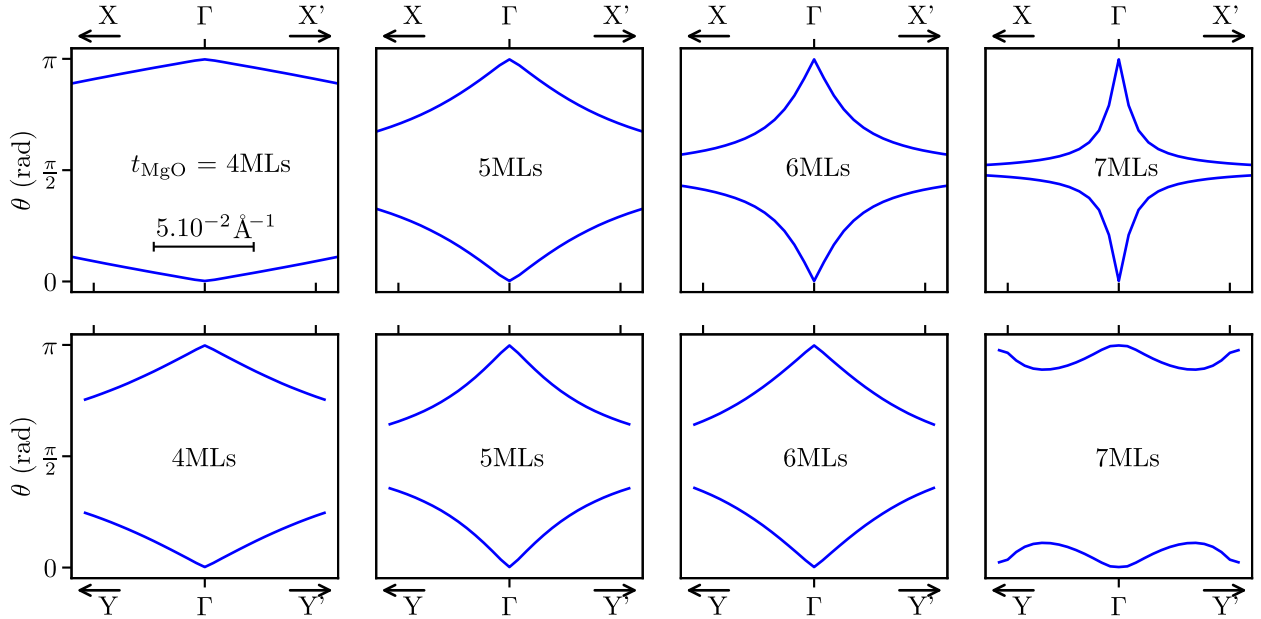


FIG. 7. Angle θ between the spin vector and the stacking axis, calculated from first principles and plotted near the top of the MoS₂ valence bands located at Γ , for Fe/MgO/MoS₂ multilayers with $t_{\text{MgO}} = 4, 5, 6$ and 7 MLs and for Bloch wave vectors along the Γ -X (upper panels) and Γ -Y (lower panels) directions.

spin either parallel or antiparallel to the exchange magnetic field (*i.e.* along the z direction), increase when the MgO-layer thickness decreases. Conversely, the built-in electric field induced by electronic reorganizations in the vdW gap and the related SOC effects tend to lay the spin in-plane and dominate magnetic proximity effects for thicker MgO layers. The variations of θ along Γ -Y

(bottom panels in Fig. 7) show similar behavior for all the MgO-layer thicknesses, except $t_{\text{MgO}} = 7$ MLs for which it does not vary monotonously with $|k_y|$, due to the interaction with the lowest energy MgO band (shown as a light line in Fig. 6).

Fig. 8 shows the modulus and direction of the in-plane projection of the spin vector, calculated for the high-

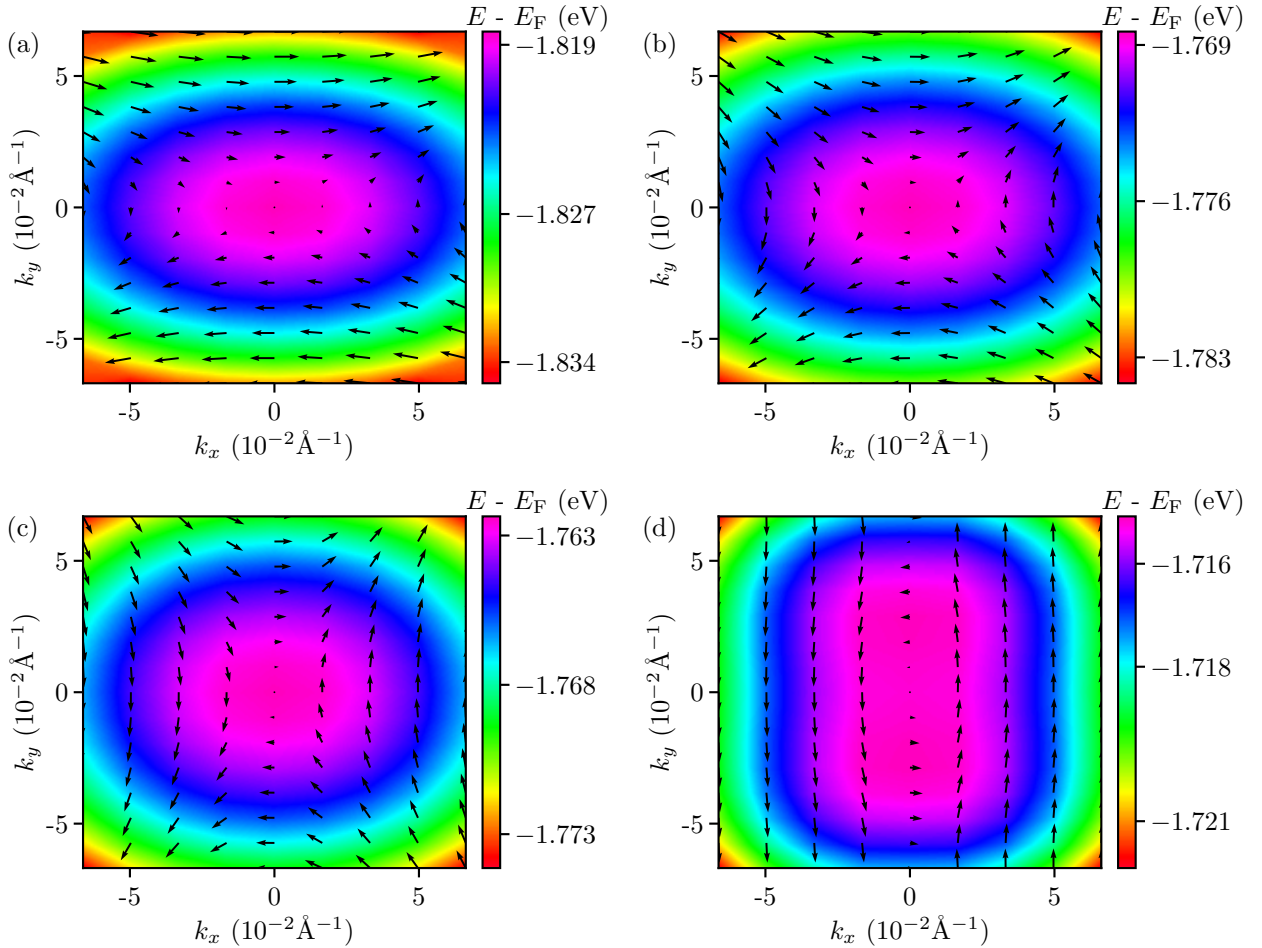


FIG. 8. Modulus and direction of the in-plane projection of the spin vector calculated near Γ from first principles, for the highest energy valence band of MoS₂ in Fe/MgO/MoS₂ multilayers with $t_{\text{MgO}} = 4$ MLs (a), 5 MLs (b), 6 MLs (c) and 7 MLs (d).

est energy MoS₂ valence band shown in Fig. 5, drawn for several values of the MgO layer thickness and as a function of k_x and k_y . The ellipsoidal shape of the constant energy lines displayed by the panels corresponding to $t_{\text{MgO}} = 4, 5$ and 6 MLs is mostly due to the anisotropy of the MgO/MoS₂ interface (which would also exist if the Fe/MgO bilayer would not be distorted). This ellipsoidal shape only disappears at the MgO layer thicknesses for which hybridization or interactions occur between MgO and MoS₂ bands. The spin texture computed for the multilayer Fe/MgO(5MLs)/MoS₂ is characteristic of that previously calculated [137, 141–145] for a 2DEG subjected to a Dresselhaus interaction [146, 147]. The spin texture is more complicated for $t_{\text{MgO}} = 4$ and 6 MLs, for which Rashba and Dresselhaus interactions may both contribute. It becomes very particular for $t_{\text{MgO}} = 7$ MLs. In this latter case, the spin vector mostly points towards the y direction. Previous studies have shown that such a nearly persistent spin texture can occur in a 2D

electron gas with the C_{2v} symmetry, when the Rashba and Dresselhaus interactions have comparable intensities [137, 141, 142, 144]. Things are more complicated for Fe/MgO/MoS₂ multilayers with the C_s symmetry: In this case, the SOC should involve more terms than the simple Rashba and Dresselhaus interactions. These two latter contributions only dominate when hybridization/interaction between MoS₂ and MgO bands is weak, which is not the case for the MgO thicknesses for which a persistent spin texture is found; additional SOC terms accounting for the MgO/MoS₂ hybridization should be considered in this case. Persistent spin textures are important for spintronic applications because they could give rise to an infinite spin lifetime [148, 149].

We have obtained similar spin textures for the second of the two highest energy splitted MoS₂ valence bands at Γ , but with an opposite direction of the in-plane projection of the spin vector.

The direction of the spin vector computed for these

two bands from first-principles (Figs. 7 and 8) can be compared to the spin texture calculated analytically using the Hamiltonian model described in Sec. III B 3. The eigenvectors with energies E_{\pm} can be used to obtain the angles θ_{\pm} (angle between the z axis and the spin vector) and ϕ_{\pm} (angle between the x axis and the projection of the spin vector in the xy plane) which give the direction of the spin vector for these 2 states. These angles are given by:

$$\theta_{+} = \text{Arctan} \left\{ \frac{\sqrt{(\alpha - \beta)^2 k_x^2 + (\alpha + \beta)^2 k_y^2}}{\mu_B B} \right\} \quad (7)$$

$$\theta_{-} = \pi - \theta_{+}$$

and

$$\tan(\phi_{+}) = \frac{(\beta - \alpha)k_x}{(\beta + \alpha)k_y} \quad (8)$$

$$\phi_{-} = \pi + \phi_{+}.$$

The good agreement between the spin-texture calculated from first-principles and the values of θ_{\pm} and ϕ_{\pm} obtained using the effective Hamiltonian is shown in Appendix A and confirms the validity of the model.

IV. COMPARISON WITH THE NON-MAGNETIC V/MgO/MoS₂ MULTILAYERS

We compare the results obtained for Fe/MgO(n MLs)/MoS₂ multilayers with the band structure and spin texture calculated for V/MgO(n MLs)/MoS₂ systems, using the same first-principles method, V being a non-magnetic $3d$ transition metal with an atomic number (23) close to that of Fe (26). V/MgO/MoS₂ multilayers thus allow to study the MgO-thickness dependence of SOC effects in a MoS₂-based stacking free of any exchange Zeeman interaction.

The dispersion of the MoS₂ valence bands is described for $t_{\text{MgO}} = 3-7$ MLs, first in a figure with a relatively large energy scale (Fig. 9), where the interfacial MgO bands are also shown. The dispersion along $\Gamma-X$ shows that a MgO band crosses the MoS₂ valence bands, as for the Fe/MgO/MoS₂ multilayers. However, this crossing occurs for thicker MgO layers in the V/MgO/MoS₂ stacking ($t_{\text{MgO}} < 5$ MLs) than in the Fe/MgO/MoS₂ multilayers ($t_{\text{MgO}} \leq 3$ MLs), the energy difference between the top of the MoS₂ and MgO valence bands being smaller for V/MgO/MoS₂ than for Fe/MgO/MoS₂. Fig. 10, which uses a smaller energy scale for $t_{\text{MgO}} = 5-7$ MLs, shows that the two MoS₂ valence bands are degenerated at Γ . The spin splitting out of Γ is proportional to the modulus of the Bloch vector, as expected for a non-magnetic two-dimensional system with a Rashba or a Dresselhaus SOC. Even for multilayers with $t_{\text{MgO}} \geq 5$ MLs, for which hybridization effects are expected to be

smaller, this spin splitting is not trivial: it increases for Bloch vectors along $\Gamma-X$ and decreases along $\Gamma-Y$, when t_{MgO} increases from 5 to 7 MLs (see Fig. 10).

The valence-band splitting shown in Fig. 10 can be fitted by an effective Hamiltonian similar to that (Eq. 1) used for studying Fe/MgO/MoS₂, but without the Zeeman term.

The parameters ϵ , m_x^* , m_y^* , α and β for which the best agreement is found between E_{\pm} and the dispersion near Γ of the MoS₂ valence bands calculated from first principles are given in Table II for the V/MgO/MoS₂ multilayers with $t_{\text{MgO}} = 5, 6$ and 7 MLs (thicknesses for which the Hamiltonian model can be used). This table shows that the Rashba and Dresselhaus parameters are greater than those calculated for the Fe/MgO/MoS₂ multilayers and that both increase when the MgO layer thickness decreases. $(\beta - \alpha)$ decreases, while $(\beta + \alpha)$ increases, when the MgO layer thickness decreases. This explains why the linear band splitting increases along $\Gamma-X$ and decreases along $\Gamma-Y$ when t_{MgO} increases from 5 to 7 MLs. The band dispersion along these two directions is indeed given by:

$$E_{\pm} = \epsilon + \frac{\hbar^2 k_x^2}{2m_x^*} \pm |(\beta - \alpha)k_x| \quad (9)$$

along $\Gamma-X$ and by

$$E_{\pm} = \epsilon + \frac{\hbar^2 k_y^2}{2m_y^*} \pm |(\beta + \alpha)k_y|. \quad (10)$$

along $\Gamma-Y$.

We have finally calculated the spin texture near the top of the valence bands of MoS₂ in V/MgO/MoS₂ multilayers with $t_{\text{MgO}} = 4-7$ MLs (see Figs. S3 and S4 in the supplementary materials file [115]). As expected, the spin vector entirely lays in the MoS₂ plane and the spin texture for the multilayers with $t_{\text{MgO}} = 6$ and 7 MLs (for which hybridization with MgO is small) is characteristic of that of a 2DEG with Dresselhaus interaction. As for Fe/MgO/MoS₂ multilayers, we found that the spin texture changes drastically for MgO thicknesses for which the MgO bands approach or cross the MoS₂ valence bands, giving rise to a nearly persistent spin texture for $t_{\text{MgO}} = 4$ MLs. The persistent spin texture obtained for $t_{\text{MgO}} = 5$ MLs is mainly due to the fact that $\alpha \approx \beta$ for this MgO thickness.

V. DISCUSSION

We must discuss the robustness of our main results and whether they would stay valid in multilayers free of any structural distortion. The increase of the SOC parameters α and β when the MgO layer thickness decreases and the corresponding Dresselhaus+Rashba-like spin texture are mostly due to the electric potential drop across the MoS₂ ML, resulting from the charge transfer in the Fe/MgO/MoS₂ and V/MgO/MoS₂ multilayers, as

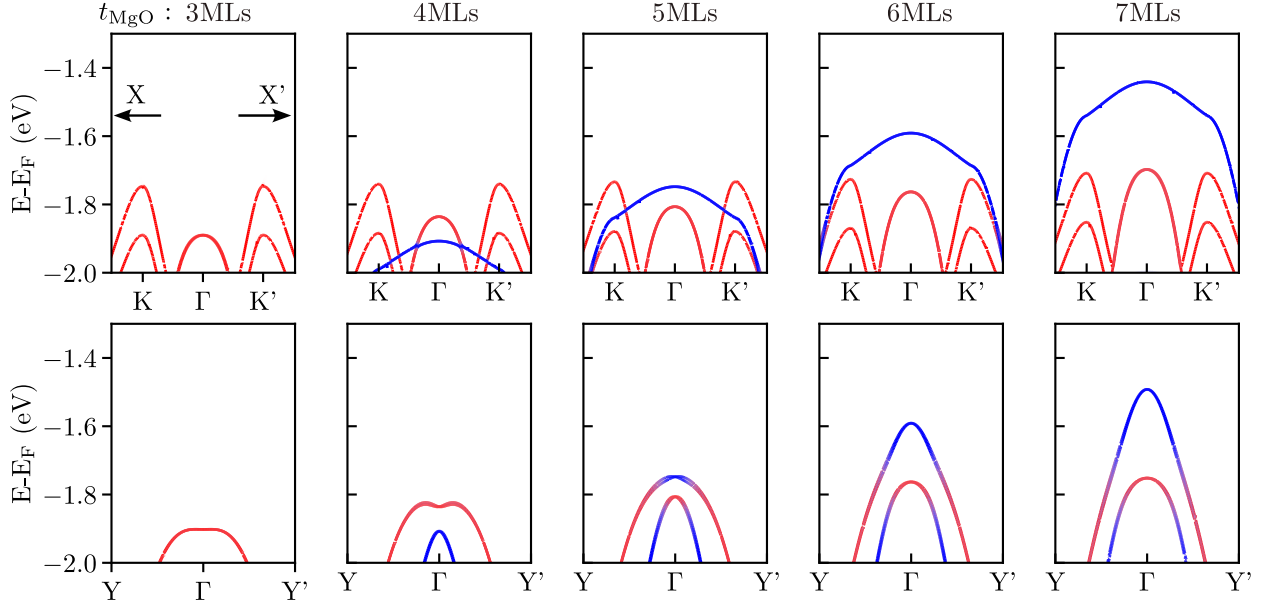


FIG. 9. Contributions of the MgO interface ML (blue lines) and of the MoS₂ ML (red lines) to the valence bands of the V/MgO/MoS₂ multilayers, for $t_{\text{MgO}} = 3, 4, 5, 6$ and 7 MLs and for Bloch wave vectors along the Γ -X (upper panels) and along the Γ -Y (lower panels) directions. The K/K' points are located between Γ and the X/X' points

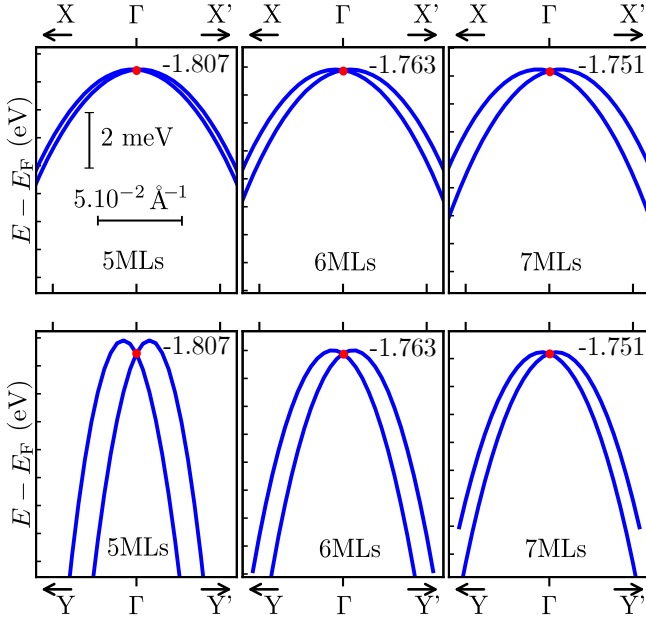


FIG. 10. Dispersion of the MoS₂ valence bands near the VBM at Γ , calculated from first principles for Bloch wave vectors along the Γ -X direction (upper panels) and along the Γ -Y direction (lower panels). The different panels correspond to V/MgO/MoS₂ multilayers with $t_{\text{MgO}} = 5, 6$ and 7 MLs. The energy of the VBM at Γ (indicated by a red dot) is given in each panel.

clearly shown in Fig. 11. These charge transfer-induced effects would also exist without structural distortion of

| t_{MgO} | 5MLs | 6MLs | 7MLs |
|---------------------------|--------|--------|--------|
| ϵ (eV) | -1.81 | -1.76 | -1.71 |
| m_x^*/m_0 | -3.584 | -3.263 | -3.175 |
| m_y^*/m_0 | -0.495 | -1.111 | -1.492 |
| α (meVÅ) | 57.3 | 14.3 | 2.86 |
| β (meVÅ) | 61.9 | 24.67 | 21.43 |
| $(\beta - \alpha)$ (meVÅ) | 4.6 | 10.37 | 18.57 |
| $(\beta + \alpha)$ (meVÅ) | 119.2 | 38.97 | 24.29 |

TABLE II. Parameters of the effective Hamiltonian achieving the best possible agreement with the MoS₂ band structure and spin texture calculated from first principles near the top of the valence bands at Γ , for V/MgO/MoS₂ multilayers with $t_{\text{MgO}} = 5, 6$ and 7 MLs.

the MgO layer, the electron transfer being mostly due (if we ignore interface effects) to the difference between the metal work function and MoS₂ electron affinity, which would keep similar values without distorting MgO [68].

Let us now focus on Fe/MgO/MoS₂ magnetic multilayers. The increase of the spin splitting near the maximum of the MoS₂ valence bands at Γ and the increase of the z component of the spin textures when the thickness of the MgO layer decreases would be preserved without distortion of the MgO layer, as it is only due to the increase of the magnetic proximity effects when the MgO spacer becomes thinner.

Fe/MgO/MoS₂ multilayers free of any distortion should thus keep being considered as versatile and adjustable systems in which the SOC and magnetic proximity effects can continuously be tuned by a judicious

choice of the MgO layer thickness.

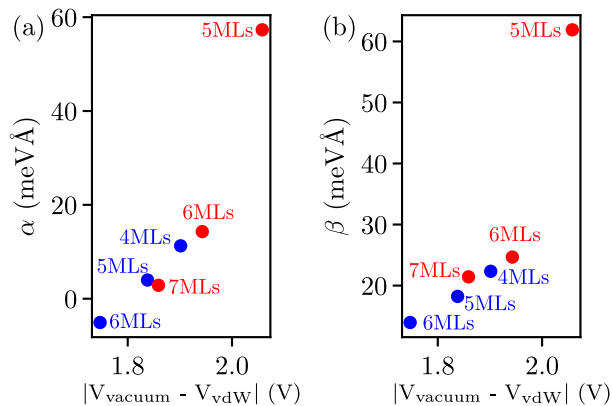


FIG. 11. Values of the SOC parameters α and β , versus the electric potential drop $|V_{\text{vacuum}} - V_{\text{vdW}}|$ calculated between the vacuum and the center of the vdW gap for Fe/MgO/MoS₂ (blue dots) and V/MgO/MoS₂ (red dots) multilayers, for different values of t_{MgO} .

However, although the electronic structure of the MgO layer does not globally change when it is distorted (the width of its band gap being nearly the same with and without distortion, see Fig. S2 in the supplementary materials file [115]), the details of the dispersion of the MgO bands along the Γ -X and Γ -Y directions are slightly modified by the crystal distortion, as it can be seen in Appendix B. This may have consequences on those of the physical properties of the MoS₂ ML which depend on the interactions or hybridization between the MgO and MoS₂ valence bands, as we have seen in Sec. III B 4. In particular, the critical MgO thicknesses below which the MgO bands cross the MoS₂ valence bands should be the same along the Γ -X and Γ -Y directions for genuine Fe/MgO/MoS₂ samples. This may slightly change the MgO thickness range where the Hamiltonian model applies, but the existence of such a MgO range is not questioned.

Finally, the persistent spin textures that we have observed for specific MgO thicknesses may also be due to the splitting of the MgO bands near Γ and to their different dispersion along Γ -X and Γ -Y: The persistent spin texture may disappear in Fe/MgO/MoS₂ multilayers (but may remain in the V/MgO/MoS₂ systems with the MgO thickness for which similar values of α and β have been found) without distorting the MgO layer. However, our results clearly show that using alternative metallic/insulating bilayers with a different band dispersion of the insulating layer along Γ -X and Γ -Y, and an insulator thickness such that the insulator valence bands cross those of the MoS₂ ML should be considered as a promising avenue to stabilize persistent spin textures in a MoS₂ ML. This would confirm that the interface symmetry can promote persistent spin textures, following sym-

metry arguments previously used to stabilize a persistent spin texture in a bulk crystal [150, 151].

VI. SUMMARY

We have investigated the electronic and magnetic properties of a MoS₂ ML in Fe(001)/MgO(n MLs)/MoS₂(1ML) stacks with $n = 3-7$. In these multilayers, the MoS₂ ML is only bound by weak vdW interaction to the Fe/MgO bilayer. An electron transfer occurs from Fe to MoS₂ in these multilayers, due to the difference between the Fe work function and MoS₂ electron affinity. We have demonstrated that the density of the corresponding 2DEG (with negligible spin-polarization) and the resulting built-in electric field in the MgO layer increase when the MgO layer thickness decreases. We have studied the splitting of the MoS₂ valence bands near Γ for these multilayers: This splitting is due to the interplay of various magnetic interactions, namely the Rashba, Dresselhaus and Zeeman interactions. Their contributions are understood by an analytical Hamiltonian model. The coefficients describing the spin-orbit and exchange-Zeeman interactions increase when the MgO layer thickness decreases, with a Dresselhaus term that dominates the Rashba one for the thinner MgO layers. As long as the MoS₂ valence bands do not interact with those of MgO, these coefficients explain the details of the dispersion, the spin texture and the rotation of the spin vector near Γ , from mostly in-plane to mostly out-of-plane when the MgO layer thickness decreases. Fe/MgO/MoS₂ multilayers with ultrathin MgO layers (1 or 2 MLs) have not been considered here. They would also deserve being studied (provide the fact that they can be grown with a high quality crystal structure), as they should show stronger magnetic proximity effects; hybridization between the MgO, MoS₂ and even Fe bands should dominate in this case. Additionally, we compared the results obtained for the magnetic Fe/MgO/MoS₂ multilayers with those calculated for non-magnetic V/MgO/MoS₂ systems, which show a different dispersion of the MoS₂ valence bands and only an in-plane spin texture, due to the absence of Zeeman effects in this case.

Van der Waals insulators like hexagonal BN could be used instead of MgO, to get thinner insulating layers between Fe and MoS₂, thus increasing the magnetic proximity effects. We finally suggest that a persistent spin texture could emerge in metal/insulator/TMDC multilayers based on an insulating layer other than MgO but with an anisotropic band dispersion and a thickness for which the insulator valence bands cross those of the MoS₂ monolayer.

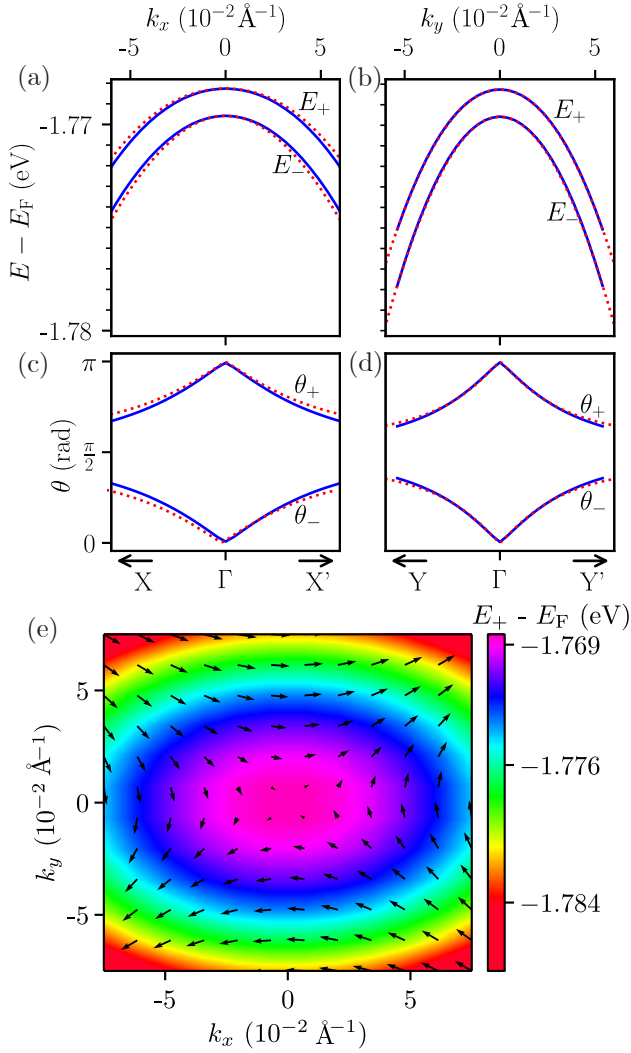


FIG. 12. (a) Dispersion of the highest-energy MoS₂ valence bands of the multilayer Fe/MgO(5MLs)/MoS₂, for Bloch vectors along Γ -X; the blue solid lines correspond to the first-principles data, while the red dotted lines correspond to the eigenvalues E_+ and E_- of the effective Hamiltonian. (b) Same as (a), but for Bloch vectors along Γ -Y. (c) Angle θ between the spin vector and the z axis, calculated for the multilayer Fe/MgO(5MLs)/MoS₂ and for Bloch vectors along Γ -X; the blue solid lines correspond to the first-principles data and the red dotted lines to the angles θ_+ and θ_- calculated from the eigenvectors of the effective Hamiltonian. (d) Same as (c), but for Bloch vectors along Γ -Y. (e) Modulus and direction of the in-plane projection of the spin vector, calculated for the multilayer Fe/MgO(5MLs)/MoS₂ using the angle ϕ_+ (Eq. 8).

Appendix A: DFT versus effective Hamiltonian

Figs. 12(a) and (b) compare the dispersion of the split MoS₂ valence bands calculated from first principles for the multilayer Fe/MgO(5MLs)/MoS₂, respectively for Bloch wave vectors along the Γ -X and Γ -Y directions of the first BZ, with the energies E_{\pm} fitted with the set of

parameters given in Table I. Figs. 12(c) and (d) compare the values of the angle θ calculated from first principles for these two bands of the same multilayer, with the angles θ_{\pm} calculated from Eq. 7 and the same set of parameters. Fig. 12(e) finally shows the modulus and direction of the projection of the spin vector in the xy -plane, calculated for Fe/MgO(5MLs)/MoS₂, using the angle ϕ_+ given in Eq. 8 and the parameters α and β previously obtained for this multilayer. All these figures show that the effective Hamiltonian correctly describes the results calculated from first principles.

Similar comparisons are given in the supplementary materials file for Fe/MgO(4MLs)/MoS₂ and Fe/MgO(6MLs)/MoS₂ (Figs. S5-S8 in [115]), and for V/MgO/MoS₂ multilayers with $t_{\text{MgO}} = 5, 6$ and 7 MLs (Figs. S9-S14 in [115]).

Appendix B: MgO band structure in the Γ -X and Γ -Y directions: cubic versus distorted bulk crystals

In this Appendix, we compare the dispersion of the bands calculated for bulk MgO along the Γ -X and Γ -Y directions of the Brillouin zone of a conventional quadratic unit cell, when the distortion described in Sec. II is taken into account and when this distortion does not occur (cubic MgO crystal with the rock-salt structure). The distortion makes the $[110]$ and $[\bar{1}\bar{1}0]$ MgO crystallographic axes non-equivalent, which lifts the degeneracy between MgO bands that would otherwise be degenerated at Γ (see Fig. 13). After this degeneracy has been lifted, the MgO valence band which has the highest energy near Γ has a stronger dispersion along Γ -Y than along Γ -X: this band corresponds to that drawn with a blue line in Fig. 6 and Fig. 9. The band which has been splitted from the former one by the structural distortion is found just below it (see Fig. 13); it shows a stronger dispersion along Γ -X than along Γ -Y. Without any distortion, these two bands are degenerate at Γ and both a dispersive band and a less dispersive one are found, with similar energies along the Γ -X and Γ -Y directions.

The band structure calculated for the distorted bulk MgO crystal explains the difference between the dispersions of the MgO valence bands calculated at the MgO/MoS₂ interface, along Γ -X and along Γ -Y.

ACKNOWLEDGMENTS

This study has been supported through the ANR Grant ANR-19-CE24-0005 and it was granted access to the HPC resources of the CALMIP supercomputing center under allocation 2021/2023-[P20042].

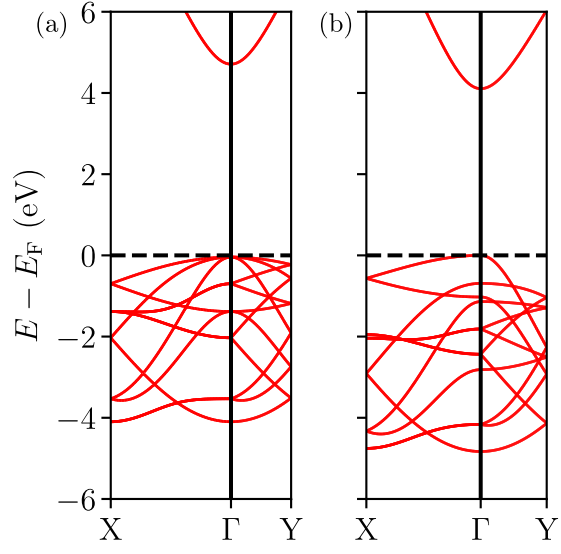


FIG. 13. Bulk MgO band structure calculated along the Γ -X and Γ -Y directions, for (a) the non-distorted cubic crystal and (b) the distorted crystal.

-
- [1] V. Podzorov, M. E. Gershenson, Ch. Kloc, R. Zeis, and E. Buchner, *Appl. Phys. Lett.* **84**, 3301 (2004).
- [2] B. Radisavljevic, A. Radenovic, J. Brivio, V. Giacometti, and A. Kis, *Nat. Nanotechnol.* **6**, 5 (2011).
- [3] L. Liu, S. B. Kumar, Y. Ouyang, and J. Guo, *IEEE Trans. Electron Devices* **58**, 3042 (2011).
- [4] Y. Yoon, K. Ganapathi, and S. Salahuddin, *Nano Lett.* **11**, 3768 (2011).
- [5] H. Fang, S. Chuang, T. C. Chang, K. Takei, T. Takahashi, and A. Javey, *Nano Lett.* **12**, 3788 (2012).
- [6] D. Lembke and A. Kis, *ACS Nano* **6**, 10070 (2012).
- [7] Q. H. Wang, K. Kalantar-Zadeh, A. Kis, J. N. Coleman, and M. S. Strano, *Nat. Nanotechnol.* **7**, 699 (2012).
- [8] S. Das, R. Gulotty, A. V. Sumant, and A. Roelofs, *Nano Lett.* **14**, 2861 (2014).
- [9] J. Kang, W. Liu, and K. Banerjee, *Appl. Phys. Lett.* **104**, 093106 (2014).
- [10] B. Radisavljevic, M. B. Whitwick, and A. Kis, *ACS Nano* **5**, 9934 (2011).
- [11] H. Wang, L. Yu, Y.-H. Lee, Y. Shi, A. Hsu, M. L. Chin, L.-J. Li, M. Dubey, J. Kong, and T. Palacios, *Nano Lett.* **12**, 4674 (2012).
- [12] P. J. Jeon, J. S. Kim, J. Y. Lim, Y. Cho, A. Pezeshki, H. S. Lee, S. Yu, S.-W. Min, and S. Im, *ACS Appl. Mater. Interfaces* **7**, 22333 (2015).
- [13] H. Wang, C. Li, P. Fang, Z. Zhang, and J. Z. Zhang, *Chem. Soc. Rev.* **47**, 6101 (2018).
- [14] W. Liu, X. Yang, Y. Zhang, M. Xu, and H. Chen, *RSC Adv.* **4**, 32744 (2014).
- [15] G. Wang, L. Bouet, M. M. Glazov, T. Amand, E. L. Ivchenko, E. Palleau, X. Marie, and B. Urbaszek, *2D Mater.* **2**, 034002 (2015).
- [16] T. A. Shastry, I. Balla, H. Bergeron, S. H. Amsterdam, T. J. Marks, and M. C. Hersam, *ACS Nano* **10**, 10573 (2016).
- [17] H. S. Lee, S.-W. Min, Y.-G. Chang, M. K. Park, T. Nam, H. Kim, J. H. Kim, S. Ryu, and S. Im, *Nano Lett.* **12**, 3695 (2012).
- [18] Z. Yin, H. Li, H. Li, L. Jiang, Y. Shi, Y. Sun, G. Lu, Q. Zhang, X. Chen, and H. Zhang, *ACS Nano* **6**, 74 (2012).
- [19] J. Miao, W. Hu, Y. Jing, W. Luo, L. Liao, A. Pan, S. Wu, J. Cheng, X. Chen, and W. Lu, *Small* **11**, 2392 (2015).
- [20] K. Dolui, A. Narayan, I. Rungger, and S. Sanvito, *Phys. Rev. B* **90**, 041401(R) (2014).
- [21] H.-C. Wu, C. Ó. Coileáin, M. Abid, O. Mauit, A. Syrlybekov, A. Khalid, H. Xu, R. Gatensby, J. Jing Wang, H. Liu, L. Yang, G. S. Duesberg, H.-Z. Zhang, M. Abid, and I. V. Shvets, *Sci. Rep.* **5**, 15984 (2015).
- [22] W. Wang, Y. Liu, L. Tang, Y. Jin, T. Zhao, and F. Xiu, *Sci. Rep.* **4**, 6928 (2015).
- [23] M. Z. Iqbal, M. W. Iqbal, S. Siddique, M. F. Khan, and S. M. Ramay, *Sci. Rep.* **6**, 21038 (2016).
- [24] H. Zhang, M. Ye, Y. Wang, R. Quhe, Y. Pan, Y. Guo, Z. Song, J. Yang, W. Guo, and J. Lu, *Phys. Chem. Chem. Phys.* **18**, 16367 (2016).
- [25] W. C. Wong, S. M. Ng, H. F. Wong, C. L. Mak, and C. W. Leung, *IEEE Trans. Magn.* **53**, 1 (2017).
- [26] A. Dankert, P. Pashaei, M. V. Kamalakar, A. P. S. Gaur, S. Sahoo, I. Rungger, A. Narayan, K. Dolui, M. A. Hoque, R. S. Patel, M. P. de Jong, R. S. Katiyar, S. Sanvito, and S. P. Dash, *ACS Nano* **11**, 6389 (2017).
- [27] K. Zhao, Y. Xing, J. Han, J. Feng, W. Shi, B. Zhang, and Z. Zeng, *J. Magn. Magn. Mater.* **432**, 10 (2017).
- [28] M. F. Khan, H. Kim, G. Nazir, S. Jung, and J. Eom, *Nanoscale* **10**, 16703 (2018).
- [29] A. Kumar and S. Choudhary, *J. Supercond. Nov. Magn.* **31**, 3245 (2018).
- [30] W. Rotjanapittayakul, W. Pijitrojana, T. Archer, S. Sanvito, and J. Prasongkit, *Sci. Rep.* **8**, 4779 (2018).
- [31] H. Lin, F. Yan, C. Hu, Q. Lv, W. Zhu, Z. Wang, Z. Wei, K. Chang, and K. Wang, *ACS Appl. Mater. Interfaces* **12**, 43921 (2020).
- [32] S. K. Behera and P. Deb, *Phys. Chem. Chem. Phys.* **22**, 19139 (2020).
- [33] A. Avsar, J. Y. Tan, T. Taychatanapat, J. Balakrishnan, G. Koon, Y. Yeo, J. Lahiri, A. Carvalho, A. S. Rodin, E. O'Farrell, G. Eda, A. H. Castro Neto, and B. Özyilmaz, *Nat Commun* **5**, 4875 (2014).
- [34] M. Gmitra and J. Fabian, *Phys. Rev. B* **92**, 155403 (2015).
- [35] Z. Wang, D.-K. Ki, J. Y. Khoo, D. Mauro, H. Berger, L. S. Levitov, and A. F. Morpurgo, *Phys. Rev. X* **6**, 041020 (2016).
- [36] W. Yan, O. Txoperena, R. Llopis, H. Dery, L. E. Hueso, and F. Casanova, *Nat. Commun.* **7**, 13372 (2016).
- [37] M. Offidani, M. Milletari, R. Raimondi, and A. Ferreira, *Phys. Rev. Lett.* **119**, 196801 (2017).
- [38] J. H. Garcia, A. W. Cummings, and S. Roche, *Nano Lett.* **17**, 5078 (2017).
- [39] A. Dankert and S. P. Dash, *Nat. Commun.* **8**, 16093 (2017).
- [40] M. Gmitra and J. Fabian, *Phys. Rev. Lett.* **119**, 146401 (2017).
- [41] S. Omar and B. J. van Wees, *Phys. Rev. B* **95**, 081404(R) (2017).
- [42] T. S. Ghiasi, A. A. Kaverzin, P. J. Blah, and B. J. van Wees, *Nano Lett.* **19**, 5959 (2019).
- [43] C. K. Safeer, J. Ingla-Aynés, F. Herling, J. H. Garcia, M. Vila, N. Ontoso, M. R. Calvo, S. Roche, L. E. Hueso, and F. Casanova, *Nano Lett.* **19**, 1074 (2019).
- [44] B. Zhao, D. Khokhriakov, Y. Zhang, H. Fu, B. Karpiak, A. M. Hoque, X. Xu, Y. Jiang, B. Yan, and S. P. Dash, *Phys. Rev. Res.* **2**, 013286 (2020).
- [45] Q. Shao, G. Yu, Y.-W. Lan, Y. Shi, M.-Y. Li, C. Zheng, X. Zhu, L.-J. Li, P. K. Amiri, and K. L. Wang, *Nano Lett.* **16**, 7514 (2016).
- [46] A. Splendiani, L. Sun, Y. Zhang, T. Li, J. Kim, C.-Y. Chim, G. Galli, and F. Wang, *Nano Lett.* **10**, 1271 (2010).
- [47] K. F. Mak, C. Lee, J. Hone, J. Shan, and T. F. Heinz, *Phys. Rev. Lett.* **105**, 136805 (2010).
- [48] Z. Y. Zhu, Y. C. Cheng, and U. Schwingenschlögl, *Phys. Rev. B* **84**, 153402 (2011).
- [49] D. Xiao, G.-B. Liu, W. Feng, X. Xu, and W. Yao, *Phys. Rev. Lett.* **108**, 196802 (2012).
- [50] K. Kosmider, J. W. Gonzalez, and J. Fernandez-Rossier, *Phys. Rev. B* **88**, 245436 (2013).
- [51] X. Xu, W. Yao, D. Xiao, and T. F. Heinz, *Nat. Phys.* **10**, 343 (2014).
- [52] H. Zeng, J. Dai, W. Yao, D. Xiao, and X. Cui, *Nat.*

- Nanotechnol. **7**, 490 (2012).
- [53] K. F. Mak, K. He, J. Shan, and T. F. Heinz, *Nat. Nanotechnol.* **7**, 494 (2012).
- [54] T. Cao, G. Wang, W. Han, H. Ye, C. Zhu, J. Shi, Q. Niu, P. Tan, E. Wang, B. Liu, and J. Feng, *Nat. Commun.* **3**, 887 (2012).
- [55] H. Yuan, X. Wang, B. Lian, H. Zhang, X. Fang, B. Shen, G. Xu, Y. Xu, S.-C. Zhang, H. Y. Hwang, and Y. Cui, *Nat. Nanotechnol.* **9**, 851 (2014).
- [56] T. Li, *Phys. Rev. B* **85**, 235407 (2012).
- [57] Q. Yue, J. Kang, Z. Shao, X. Zhang, S. Chang, G. Wang, S. Qin, and J. Li, *Phys. Lett. A* **376**, 1166 (2012).
- [58] Q. Zhang, Y. Cheng, L.-Y. Gan, and U. Schwingenschlöggl, *Phys. Rev. B* **88**, 245447 (2013).
- [59] H. Shi, H. Pan, Y.-W. Zhang, and B. I. Yakobson, *Phys. Rev. B* **87**, 155304 (2013).
- [60] L. Wang, A. Kutana, and B. I. Yakobson, *Ann. Phys.* **526**, L7 (2014).
- [61] Moh. Adhib Ulil Absor, H. Kotaka, F. Ishii, and M. Saito, *Phys. Rev. B* **94**, 115131 (2016).
- [62] R. K. Defo, S. Fang, S. N. Shirodkar, G. A. Tritsarlis, A. Dimoulas, and E. Kaxiras, *Phys. Rev. B* **94**, 155310 (2016).
- [63] N. Zibouche, P. Philippsen, T. Heine, and A. Kuc, *Phys. Chem. Chem. Phys.* **16**, 11251 (2014).
- [64] C. Cheng, J.-T. Sun, X.-R. Chen, H.-X. Fu, and S. Meng, *Nanoscale* **8**, 17854 (2016).
- [65] Y. Affandi, M. A. U. Absor, and K. Abraha, *J. Phys. Conf. Ser.* **1011**, 012070 (2018).
- [66] Y. Affandi and M. A. Ulil Absor, *Phys. E Low-Dimens. Syst. Nanostructures* **114**, 113611 (2019).
- [67] Q. Zhang, S. A. Yang, W. Mi, Y. Cheng, and U. Schwingenschlöggl, *Adv. Mater.* **28**, 959 (2016).
- [68] Z. Zhou, P. Marcon, X. Devaux, P. Pigeat, A. Bouché, S. Migot, A. Jaafar, R. Arras, M. Vergnat, L. Ren, H. Tornatzky, C. Robert, X. Marie, J.-M. George, H.-Y. Jaffrès, M. Stoffel, H. Rinnert, Z. Wei, P. Renucci, L. Calmels, and Y. Lu, *ACS Appl. Mater. Interfaces* **13**, 32579 (2021).
- [69] Y. Li, J. Ludwig, T. Low, A. Chernikov, X. Cui, G. Arefe, Y. D. Kim, A. M. van der Zande, A. Rigosi, H. M. Hill, S. H. Kim, J. Hone, Z. Li, D. Smirnov, and T. F. Heinz, *Phys. Rev. Lett.* **113**, 266804 (2014).
- [70] A. Kormányos, V. Zólyomi, N. D. Drummond, and G. Burkard, *Phys. Rev. X* **4**, 011034 (2014).
- [71] D. MacNeill, C. Heikes, K. F. Mak, Z. Anderson, A. Kormányos, V. Zólyomi, J. Park, and D. C. Ralph, *Phys. Rev. Lett.* **114**, 037401 (2015).
- [72] K. V. Shanavas and S. Satpathy, *Phys. Rev. B* **91**, 235145 (2015).
- [73] G. Aivazian, Z. Gong, A. M. Jones, R.-L. Chu, J. Yan, D. G. Mandrus, C. Zhang, D. Cobden, W. Yao, and X. Xu, *Nat. Phys.* **11**, 148 (2015).
- [74] A. Srivastava, M. Sidler, A. V. Allain, D. S. Lembke, A. Kis, and A. Imamoglu, *Nat. Phys.* **11**, 141 (2015).
- [75] A. Kuc and T. Heine, *Chem. Soc. Rev.* **44**, 2603 (2015).
- [76] L.-Y. Gan, Q. Zhang, Y. Cheng, and U. Schwingenschlöggl, *Phys. Rev. B* **88**, 235310 (2013).
- [77] Q. Chen, Y. Ouyang, S. Yuan, R. Li, and J. Wang, *ACS Appl. Mater. Interfaces* **6**, 16835 (2014).
- [78] N. Feng, W. Mi, Y. Cheng, Z. Guo, U. Schwingenschlöggl, and H. Bai, *ACS Appl. Mater. Interfaces* **6**, 4587 (2014).
- [79] M. Yin, X. Wang, W. Mi, and B. Yang, *Comput. Mater. Sci.* **99**, 326 (2015).
- [80] J. Qi, X. Li, Q. Niu, and J. Feng, *Phys. Rev. B* **92**, 121403(R) (2015).
- [81] Y. Ye, J. Xiao, H. Wang, Z. Ye, H. Zhu, M. Zhao, Y. Wang, J. Zhao, X. Yin, and X. Zhang, *Nat. Nanotechnol.* **11**, 598 (2016).
- [82] O. L. Sanchez, D. Ovchinnikov, S. Misra, A. Allain, and A. Kis, *Nano Lett.* **16**, 5792 (2016).
- [83] B. Liu, L.-J. Wu, Y.-Q. Zhao, L.-Z. Wang, and M.-Q. Cai, *Eur. Phys. J. B* **89**, 80 (2016).
- [84] D. Zhong, K. L. Seyler, X. Linpeng, R. Cheng, N. Sivadas, B. Huang, E. Schmidgall, T. Taniguchi, K. Watanabe, M. A. McGuire, W. Yao, D. Xiao, K.-M. C. Fu, and X. Xu, *Sci. Adv.* **3**, e1603113 (2017).
- [85] T. Garandel, R. Arras, X. Marie, P. Renucci, and L. Calmels, *Phys. Rev. B* **95**, 075402 (2017).
- [86] K.-A. Min, J. Cha, K. Cho, and S. Hong, *2D Mater.* **4**, 024006 (2017).
- [87] D. Somvanshi, S. Kallatt, C. Venkatesh, S. Nair, G. Gupta, J. K. Anthony, D. Karmakar, and K. Majumdar, *Phys. Rev. B* **96**, 205423 (2017).
- [88] Y. Song, X. Wang, and W. Mi, *Adv. Electron. Mater.* **3**, 1700245 (2017).
- [89] C. Zhao, T. Norden, P. Zhang, P. Zhao, Y. Cheng, F. Sun, J. P. Parry, P. Taheri, J. Wang, Y. Yang, T. Scrace, K. Kang, S. Yang, G.-x. Miao, R. Sabirianov, G. Kioseoglou, W. Huang, A. Petrou, and H. Zeng, *Nat. Nanotechnol.* **12**, 757 (2017).
- [90] X. Xue, X. Wang, and W. Mi, *J. Phys. Appl. Phys.* **52**, 115303 (2019).
- [91] T. Norden, C. Zhao, P. Zhang, R. Sabirianov, A. Petrou, and H. Zeng, *Nat. Commun.* **10**, 4163 (2019).
- [92] C. Lin, Y. Li, Q. Wei, Q. Shen, Y. Cheng, and W. Huang, *ACS Appl. Mater. Interfaces* **11**, 18858 (2019).
- [93] M. Ge, Y. Su, H. Wang, G. Yang, and J. Zhang, *RSC Adv.* **9**, 14766 (2019).
- [94] K. Zollner, P. E. Faria Junior, and J. Fabian, *Phys. Rev. B* **100**, 085128 (2019).
- [95] J. Xie, L. Jia, H. Shi, D. Yang, and M. Si, *Jpn. J. Appl. Phys.* **58**, 010906 (2019).
- [96] D. Zhong, K. L. Seyler, X. Linpeng, N. P. Wilson, T. Taniguchi, K. Watanabe, M. A. McGuire, K.-M. C. Fu, D. Xiao, W. Yao, and X. Xu, *Nat. Nanotechnol.* **15**, 187 (2020).
- [97] Y. Zhang, K. Shinokita, K. Watanabe, T. Taniguchi, M. Goto, D. Kan, Y. Shimakawa, Y. Moritomo, T. Nishihara, Y. Miyauchi, and K. Matsuda, *Adv. Mater.* **32**, 2003501 (2020).
- [98] K. Zollner, P. E. Faria Junior, and J. Fabian, *Phys. Rev. B* **101**, 085112 (2020).
- [99] E. Rashba and F. T. Tela, *Solid State* **2**, 1224 (1960).
- [100] Y. A. Bychkov and E. I. Rashba, *J. Phys. C Solid State Phys.* **17**, 6039 (1984).
- [101] A. Manchon, H. C. Koo, J. Nitta, S. M. Frolov, and R. A. Duine, *Nat. Mater.* **14**, 871 (2015).
- [102] G. Bihlmayer, O. Rader, and R. Winkler, *New J. Phys.* **17**, 050202 (2015).
- [103] H. W. Yeom and M. Grioni, *J. Electron Spectrosc. Relat. Phenom.* **201**, 2 (2015).
- [104] G. Bihlmayer, P. Noël, D. V. Vyalikh, E. V. Chulkov, and A. Manchon, *Rev Pys* **4**, 642 (2022).
- [105] Y. C. Cheng, Z. Y. Zhu, M. Tahir, and U. Schwingenschlöggl, *EPL* **102**, 57001 (2013).

- [106] Q.-F. Yao, J. Cai, W.-Y. Tong, S.-J. Gong, J.-Q. Wang, X. Wan, C.-G. Duan, and J. H. Chu, *Phys. Rev. B* **95**, 165401 (2017).
- [107] M. A. U. Absor, I. Santoso, Harsojo, K. Abraha, H. Kotaka, F. Ishii, and M. Saito, *J. Appl. Phys.* **122**, 153905 (2017).
- [108] Moh. Adhib Ulil Absor, H. Kotaka, F. Ishii, and M. Saito, *Jpn. J. Appl. Phys.* **57**, 04FP01 (2018).
- [109] T. Hu, F. Jia, G. Zhao, J. Wu, A. Stroppa, and W. Ren, *Phys. Rev. B* **97**, 235404 (2018).
- [110] J. Chen, K. Wu, H. Ma, W. Hu, and J. Yang, *RSC Adv.* **10**, 6388 (2020).
- [111] P. A. L. Sino, L.-Y. Feng, R. A. B. Villaos, H. N. Cruzado, Z.-Q. Huang, C.-H. Hsu, and F.-C. Chuang, *Nanoscale Adv.* **3**, 6608 (2021).
- [112] K. Lee, W. S. Yun, and J. D. Lee, *Phys. Rev. B* **91**, 125420 (2015).
- [113] L. Xiang, Y. Ke, and Q. Zhang, *Appl. Phys. Lett.* **115**, 203501 (2019).
- [114] J. Schliemann and D. Loss, *Phys. Rev. B* **68**, 165311 (2003).
- [115] See Supplemental Material at ... to be completed
- [116] T. Urano and T. Kanaji, *J. Phys. Soc. Jpn.* **57**, 3403 (1988).
- [117] J. Neugebauer and M. Scheffler, *Phys. Rev. B* **46**, 16067 (1992).
- [118] G. Kresse and J. Hafner, *Phys. Rev. B* **47**, 558 (1993).
- [119] G. Kresse and J. Hafner, *Phys. Rev. B* **49**, 14251 (1994).
- [120] G. Kresse and J. Furthmüller, *Computational Materials Science* **6**, 15 (1996).
- [121] G. Kresse and J. Furthmüller, *Phys. Rev. B* **54**, 11169 (1996).
- [122] P. E. Blöchl, *Phys. Rev. B* **50**, 17953 (1994).
- [123] J. P. Perdew, K. Burke, and M. Ernzerhof, *Phys. Rev. Lett.* **77**, 3865 (1996).
- [124] S. Grimme, J. Antony, S. Ehrlich, and H. Krieg, *J. Chem. Phys.* **132**, 154104 (2010).
- [125] S. Steiner, S. Khmelevskiy, M. Marsmann, and G. Kresse, *Phys. Rev. B* **93**, 224425 (2016).
- [126] H. J. Monkhorst and J. D. Pack, *Phys. Rev. B* **13**, 5188 (1976).
- [127] U. Herath, P. Tavazde, X. He, E. Bousquet, S. Singh, F. Muñoz, and A. H. Romero, *Comput. Phys. Commun.* **251**, 107080 (2020).
- [128] H. Chen, J. Zhao, X. Wang, X. Chen, Z. Zhang, and M. Hua, *Nanoscale* **14**, 5551 (2022).
- [129] R. E. Simon, *Phys. Rev.* **116**, 613 (1959).
- [130] S. McDonnell, A. Azcatl, R. Addou, C. Gong, C. Battaglia, S. Chuang, K. Cho, A. Javey, and R. M. Wallace, *ACS Nano* **8**, 6265 (2014).
- [131] S. L. Howell, D. Jariwala, C.-C. Wu, K.-S. Chen, V. K. Sangwan, J. Kang, T. J. Marks, M. C. Hersam, and L. J. Lauhon, *Nano Lett.* **15**, 2278 (2015).
- [132] J. Fontanella, C. Andeen, and D. Schuele, *J. Appl. Phys.* **45**, 2852 (1974).
- [133] V. K. Dugaev, P. Bruno, M. Taillefumier, B. Canals, and C. Lacroix, *Phys. Rev. B* **71**, 224423 (2005).
- [134] T. S. Nunner, N. A. Sinitsyn, M. F. Borunda, V. K. Dugaev, A. A. Kovalev, A. Abanov, C. Timm, T. Jungwirth, J. I. Inoue, A. H. MacDonald, and J. Sinova, *Phys. Rev. B* **76**, 235312 (2007).
- [135] T. Kato, Y. Ishikawa, H. Itoh, and J. I. Inoue, *Phys. Rev. B* **77**, 233404 (2008).
- [136] I. A. Ado, I. A. Dmitriev, P. M. Ostrovsky, and M. Titov, *Phys. Rev. Lett.* **117**, 046601 (2016).
- [137] S. D. Ganichev and L. E. Golub, *Phys. Status Solidi B* **251**, 1801 (2014).
- [138] Y. Y. Tkach, *Phys. Status Solidi B* **258**, 2000553 (2021).
- [139] M. Studer, M. P. Walsler, S. Baer, H. Rusterholz, S. Schön, D. Schuh, W. Wegscheider, K. Ensslin, and G. Salis, *Phys. Rev. B* **82**, 235320 (2010).
- [140] A. Krzyżewska and A. Dyrdał, *Physica E: Low-dimensional Systems and Nanostructures* **135**, 114961 (2022).
- [141] S. D. Ganichev and W. Prettl, *J. Phys. Condens. Matter* **15**, R935 (2003).
- [142] S.-Q. Shen, *Phys. Rev. B* **70**, 081311(R) (2004).
- [143] B. A. Bernevig, J. Orenstein, and S.-C. Zhang, *Phys. Rev. Lett.* **97**, 236601 (2006).
- [144] Z. Li, F. Marsiglio, and J. P. Carbotte, *Sci. Rep.* **3**, 2828 (2013).
- [145] X. Li, H. Tian, H. J. Zhao, C. Xu, M. Ye, L. Chen, H. Xiang, J.-M. Liu, L. Bellaiche, D. Wu, and Y. Yang, *Phys. Rev. B* **106**, L201105 (2022).
- [146] G. Dresselhaus, *Phys. Rev.* **100**, 580 (1955).
- [147] M. I. Dyakonov, *Sov. Phys. Semicond.* **20**, 110 (1986).
- [148] N. S. Averkiev and L. E. Golub, *Semicond. Sci. Technol.* **23**, 114002 (2008).
- [149] J. D. Koralek, C. P. Weber, J. Orenstein, B. A. Bernevig, S.-C. Zhang, S. Mack, and D. D. Awschalom, *Nature* **458**, 610 (2009).
- [150] L. L. Tao and E. Y. Tsymbal, *Nat. Commun.* **9**, 2763 (2018).
- [151] H. J. Zhao, H. Nakamura, R. Arras, C. Paillard, P. Chen, J. Gosteau, X. Li, Y. Yang, and L. Bellaiche, *Phys. Rev. Lett.* **125**, 216405 (2020).